Asymmetric Ionospheric Equivalent Currents at Magnetic Conjugate Points

by

Bjørn Rosland

A thesis submitted in fulfilment for the
Master's degree in Space Physics

in the
Faculty of Mathematics and Natural Science
Birkeland Center for Space Science

June 2017

UNIVERSITY OF BERGEN

Abstract

Faculty of Mathematics and Natural Science
Birkeland Center for Space Science

Master of Science

by Bjørn Rosland

In this thesis we will study high-latitude ionospheric equivalent currents at magnetic conjugate points. The following questions have been addressed in this thesis: What solar zenith angle defines the dark-sunlit terminator? How does the IMF By component affect the correlation between nominal conjugate points? How does the geomagnetic field affect current identities. We will study equivalent currents from their induced magnetic disturbances provided by SuperMAG. SuperMAG provides large dataset covering more than 30 years from more than 400 magnetometers. Interplanetary magnetic field data were provided by NASA OMNIweb from the satellites ACE, IMP-8, Geotail and WIND. Pairs of nominal conjugate stations have been identified and the data have been transformed into appropriate apex quasi-dipole coordinate system. Magnetic perturbation data was used to identify the sunlit-darkness for each magnetometer stations. We found that IMF control of magnetic field lines worsen the correlation of magnetic perturbations, which is probably due to asymmetric currents associated with IMF B_y. Ionospheric conductance has been reported to be scaled with the strength of the magnetic field, which is consistent with our results. We were able to derive an method of determining the scaling factor, but some caution should be used with this result due to statistical uncertainties in our data set.

Acknowledgements

Contents

List of Figures

List of Tables

Abbreviations

GSM	Geocentric Solar Magnetic
HCS	Heliospheric Current Sheet
IAGA	International Association of Geomagnetism and Aeronomy
IGRF	International Geomagnetic Reference Field
IGRF	International Reference Ionosphere
IMF	Interplanetary Magnetic Field
MLT	Magnetic Local Time
NH	Northern Hemisphere
SH	Southern Hemisphere
QD	Quasi-Diple
UT	Universal Time

Physical Constants

Elementary charge	e	$=$	1.602×10^{-19} C
Earth mean radius	R_E	$=$	6371.009 km
Earth equatorial radius	R_{eq}	$=$	6378.1370 km
Magnetic permeability	μ_0	$=$	$4\pi \times 10^{-7} \mathrm{Hm}^{-1}$
Vacuum permittivity	ϵ_0	$=$	8.854×10^{-12} F/m

Symbols

$\mathbf{f}_i$	Quasi-Dipole base vector (i=1,2,3)	
$\mathbf{B}$	magnetic field	T
$\mathbf{E}$	electric field	Vm^{-1}
$\mathbf{v}$	plasma velocity	ms^{-1}
V	magnetic potential	
n	number density	m^{-3}
h	geodetic height	km
h_a	field line height	km
S_a	solar radio flux at 10.7 cm	$10^{-22}\mathrm{Wm}^{-2}\mathrm{Hz}^{-1}$
ω_g	gyrofrequency	Hz
ν	collision frequency	Hz
μ	magnetic moment	J/T
λ	geographic latitude	°
φ	geographic longitude	°
λ_a	apex latitude	°
φ_a	apex longitude	°
λ_{qd}	QD latitude	°
φ_{qd}	QD longitude	°
ϕ	electric potential	
χ	solar zenith angle	°
σ_P	Pedersen conductivity	Sm^{-1}
σ_H	Hall conductivity	Sm^{-1}
Σ_P	Pedersen conductance	S
Σ_H	Hall conductance	S

Chapter 1

Introduction

The ionosphere is a region in the upper atmosphere which is able to carry electrical current which can be registered on the ground as disturbances in the magnetic field. For this reason ground based magnetometers have been placed all over the globe to monitor the ionospheric current systems. This thesis focus on current systems in the high latitude ionosphere which is coupled to the solar wind and interplanetary magnetic field. This currents system originates from a process of convecting plasma set in motion of a cycle of merging and reconnection of magnetic field lines tied to the solar wind. This current system is mirrored in the hemispheres, but asymmetries exist. Not all currents are registered by ground based magnetometers and we are therefore limited to study currents visible to magnetometers. Such currents are referred as equivalent currents and are the main topic for this thesis. Several factors contribute to asymmetric features which we have studied using magnetic perturbation data provided by SuperMAG and converted into apex quasi-dipole coordinate system.

In the Theory chapter 2 we give a brief introduction to the formation of the ionosphere followed by sections on the solar wind-magnetosphere-ionosphere coupling. We have also discussed how magnetic perturbation are measured and give a precise definition of equivalent currents. The equivalents behave differently in sunlit and dark conditions and we will see that ionospheric conductance gradient at the terminator leads to currents which is not physically possible. Finally, we will discuss asymmetries associated with the interplanetary magnetic field and differences in magnetic field strengths at conjugate points. In chapter 3 we give introduce our datasets provided by SuperMAG (magnetic perturbation data) and OMNIWeb (satellite measurements of the interplanetary magnetic field). The next chapter (Chapter 4), deals with data processing and coordinate transformation. Our results and discussion can be found in Chapter 5. In the final chapter (Chapter 6) we summarize our findings and conclusions.

The determination of which solar zenith angle that defines darkness was approached using two methods. In the first method we used a simple model of the ionosphere to determined how many degrees below the horizon is necessary to be in darkness. The second method involved identifying at which solar zenith angles magnetic perturbation were highly correlated. We used IMF control of magnetic foot point to improve conjugacy of the magnetic stations pairs expecting increased correlation. However, we did not find any indication that this was the case, rather the opposite. Our explanation for this result is that magnetic perturbation vectors point in different directions with respect to each other between the hemispheres due to asymmetric current systems associated with the IMF B_y. Ionospheric conductance has been showed to be scaled with the strength of the magnetic field, and we found a possible scaling factor from our data sets. However, some cautions should be considered with this result.

Chapter 2

Theory

At the beginning of the 20th century it was realized that currents in the upper atmosphere at auroral latitudes could be described as two-cell pattern with respect to the Sun (Birkeland [6]). This is now understood as a process liked to a cycle of open and closed magnetic flux (Dungey [17]) and ground based magnetometers have been used to monitor ionospheric currents and geomagnetic disturbances. According to the Fukushima theorem (Fukushima [23]) only the divergence-free part of horizontal ionospheric currents are visible to ground magnetometers at high latitudes. This is a useful concept in the discussion of equivalent currents which is used to describe ionospheric currents at high latitudes. Using a chain of ground based magnetometers along the Greenland coast Friis-Christensen et al. [21] were able to make a map of equivalent current pattern in the northern hemisphere. Which ionospheric currents are associated with the equivalent pattern is determined by the ionospheric conductivity and Laundal et al. [43, 44] found that in the sunlit ionosphere currents resemble Hall currents while in the dark ionosphere is the currents system influenced by Birkeland currents. Several ionospheric conductance models have been suggested (Moen and Brekke [49]) but these models are simplifications, since they leads to infinite conductance gradients at the day-night terminator. Asymmetries in ionospheric convection (e.g. Cowley [13], Cowley and Lockwood [14], Cowley et al. [15], Heppner [30], Tenfjord et al. [65]) and shift of magnetic foot points Østgaard et al. [50, 51] are associated with the interplanetary magnetic field which may have an influence on the equivalent currents at conjugate points. Asymmetries in ionospheric currents have also been linked to the difference in magnetic and geographic pole offset, and the difference in magnetic field strength at magnetic conjugate points (Laundal and Richmond [42]). The ionospheric conductance have also been reported to be scaled with the strength of the magnetic field (e.g. Cnossen et al. [12], Richmond [57]).

2.1   The Ionosphere

The ionosphere is a region in the upper atmosphere consisting of ionised particles and electrons. The ionosphere is formed by EUV-radiation emitted by the Sun (photo-ionization) on the dayside and mostly by energetic particle precipitation on the nightside (Rees [55]). When electrons are detached from its molecule the process is called ionization, and when the opposite process occur, an electron attaches to an ionized particle forming an neutral particle, this process is called recombination. Ions and electrons are often near photochemical equilibrium in the ionosphere, which means that the chemical production rate is balanced with the chemical loss rate (Richmond [57])
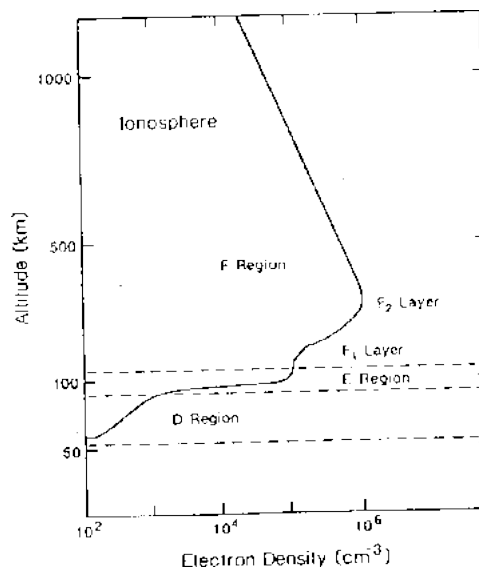
FIGURE 2.1: The density profile of the ionosphere
http://www.physics.usyd.edu.au/ cairns/teaching/lecture16/img71.gif

The ionosphere is dived into several layers where electron densities reaches local maxima which is referred as D, E and F-layer. The D-layer lies below 90 km altitude where photoionization of NO by atomic hydrogen Lyman-α is the dominant ionization source. This layer does only exist during daytime. The layer above, E-layer, lies between 90-150 km altitude while the F-layer lies between 150-500 km. Near the peak of the F-layer plasma constitutes mostly of O^+ and below the peak NO^+ and O^+ are the dominant ions. During night-time the F-layer is split into F1 and F2 layer. The ionosphere has different structure during daytime and night-time due to different light conditions and molecule mixture (Kelly [34]).

In the E-region ions and electrons are affected by atmospheric winds and dynamics. The winds forces the ions to move across the geomagnetic field while electrons moves at right angles to both the magnetic field and the ion motion. This causes charge separations
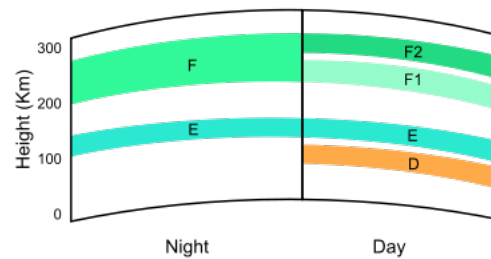
FIGURE 2.2: The ionosphere is divided into several layers. During daytime the F layer is split into two layers, F1 and F2. Additionally the D-layer emerges
`https://commons.wikimedia.org/wiki/File:IonosphereLayers-NPS.gif`

which again generates electric currents. This is a dynamo effect and this region is therefore referred as the *dynamo layer*. During daytime the atmosphere experience thermal expansion by solar radiation and compress during during night-time. This causes tidal motion which give rise to the *solar quiet current system* or S_q-currents at mid-latitudes. This current system has two vortices, one in the northern hemisphere and another in the southern hemisphere and due to the Coriolis effect they flow in opposite directions. At the equator these currents touch each other, and combined with the geometry of the geomagnetic field and nearly perpendicular incidence solar rays, the conductivity is enhances forming the *equatorial electrojets* (Baumjohann and Treumann [4]).

At high-latitudes particle precipitation causes enhanced ionization leading to higher conductivity in the aurora oval. The high conductivity give rise to the *auroral electrojets*. These currents flows just above 100 km altitude and can be detected on the ground as disturbances in the magnetic field. The *AE*-index has been developed to detect the electrojets (Davis and Sugiura [16]). The auroral electrojet is actually a combination of a electrojet flowing in the westward direction, the westward electrojet, and another in the eastward direction, the eastward electrojet.

2.2   The Solar Wind

The ultimate source of convection and currents in the ionosphere comes from the solar wind which acts as an electric generator and adds energy to the ionosphere. The solar wind is a stream of particles ejected from the solar corona. A typical speed for the solar wind is 500 km/s. The Sun rotates around its axis with a 27 day rotation rotation period. As the solar wind expands the solar wind is spiralling out of the Sun as seen from the ecliptic plane. This phenomenon is known as the *Parker spiral* (Parker [52]) The

magnetic field lines in the interplanetary magnetic field (IMF) are tied to the particles in the solar wind, which is known as the "frozen-in" concept or Alfven's Theorem (Alfvén [2]). As the solar wind expands radially from the Sun the IMF is stretched into a shape similar to a ballerina skirt. According to Amperes law $\nabla \times \mathbf{B} = \mu_0 \mathbf{j}$ there exist a current sheet associated with the IMF known as the *Heliospheric Current Sheet* (HCS)(Smith [63]). A 3D-model of the Parker spiral and the HCS is shown in Figure 2.3.
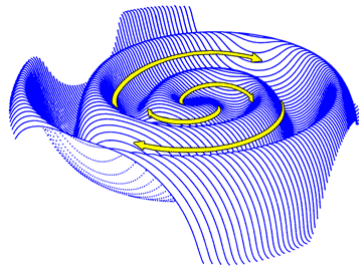
FIGURE 2.3: The yellow arrows represents the Parker spiral and the blue sheets represents the HCS and the associated magnetic field `https://helios.gsfc.nasa.gov/solarmag.html`

As the Earth orbits around the Sun it will alternately lie above and below the HCS and will also experience to different orientations of the IMF. When the IMF is anti-parallel with the terrestrial magnetic field then magnetic reconnection occurs and sets in motion the ionospheric convection discussed in section 2.5. Additionally, the east-west component of the IMF, or IMF B_y will be different during the orbit. IMF B_y is associated with several asymmetric features in the morphology and electrodynamics in the ionosphere discussed in section 2.13.

2.3   The Magnetosphere

The magnetosphere is a volume of space surrounding the Earth where the terrestrial magnetic field dominates. When the solar wind collides with the magnetic field of the Earth, the shape of the geomagnetic field is then distorted. On the dayside, the geomagnetic field is compressed by hydrodynamic pressure from the solar wind. The distance to the boundary of the magnetosphere, the magnetopause, lies where the pressure from the solar wind is balanced by the magnetic pressure from the geomagnetic field. The geomagnetic field is elongated into tear drop shape on the nightside forming the magnetotail. The bow shock is the outermost layer of the magnetopause (Baumjohann and Treumann [4], Kelly [34]). An illustration of the structure of the magnetosphere is shown is Figure 2.4. Discussion on the topic of magnetospheres are given by Blanc et al. [9] and Kivelson [37].
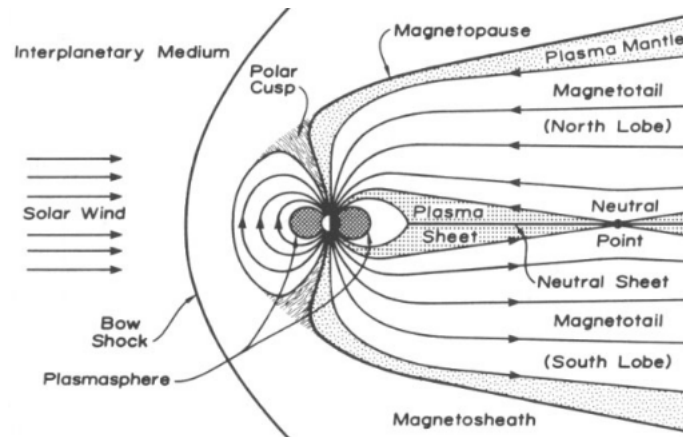
FIGURE 2.4: An illustration of the structure of the magnetosphere.
Figure by Kivelson [37]

The magnetic field lines in the IMF cannot penetrate into the magnetosphere. When the IMF is in contact with the geomagnetic field they reconnect and is transported over the nightside where they reconnect again in a process called the *Dungey cycle*.

2.4 The Dungey Cycle

The high-latitude ionospheric convection and currents are driven by a process of magnetic reconnection first described by Dungey [17]. In section 2.2 we discussed that charged particles are ejected from the Sun and flows as a plasma towards the Earth. The IMF is frozen to the ejected particles and dragged along with the plasma flow. When the IMF is southward the IMF will reconnect with the magnetic field lines of the Earth on the dayside. The terrestrial magnetic field lines are now connected with the IMF and transported over the nightside where the magnetic field lines reconnects again in the magnetotail. Magnetic tension forces the magnetic field lines back to the dayside and the process repeats itself. This is known as the Dungey cycle. This is illustrated in Figure 2.5.
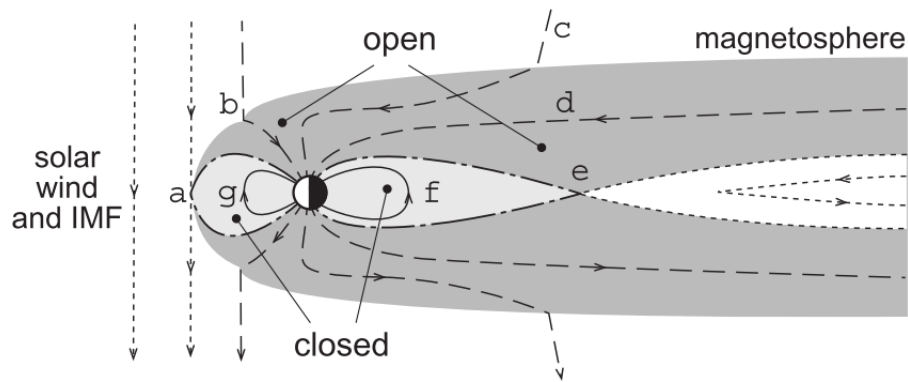
FIGURE 2.5: The numbers indicates sequential times of the magnetic field lines. At (a) is the IMF and the terrestrial magnetic field lines anti-parallel and connects. The solar wind moves the magnetic field lines anti-sunward from (b) to (d) and magnetic field lines reconnects again in point (e). The terrestrial magnetic field lines are anchored to the Earth and magnetic tension forces the magnetic field lines sunward from (f) to (g). When the magnetic field lines eventually reaches (a) again and the process is repeated. Figure from Milan et al. [48]

Here the frozen-in concept of magnetic field lines and plasma is important. As the magnetic field lines are set in motion by the Dungey cycle plasma is moved along with it. This gives rise to plasma convection (section 2.5) which is the basis for high-latitude electrodynamics.

Magnetic field lines connected to the IMF are called *open magnetic field lines* ((b), (c) and (d) in Figure 2.5) while magnetic field lines with both foot points to the Earth are called *closed magnetic field lines* ((f) and (g) in Figure 2.5). The area with open field lines is called the polar cap.

2.5   Ionospheric Convection

In the theory of *magnetohydro dynamics* (MHD) plasma is idealized to have infinite electrical conductivity and it can be showen by non-relativistic Lorentz transformation that an observer on an Earth fixed frame will observe an electric field given by

$$\mathbf{E} = -\mathbf{v} \times \mathbf{B} \tag{2.1}$$

where $\mathbf{v}$ is the velocity of the plasma flow and $\mathbf{B}$ is the magnetic field. An equivalent statement is that the plasma drift with an velocity

$$\mathbf{v} = \frac{\mathbf{E} \times \mathbf{B}}{B^2} \tag{2.2}$$

which is often referred as E×B-drift. The magnetic field lines are pointing downwards in NH and when the plasma flow is anti-sunward then it is possible to show that the electric field across the polar cap E_{pc} points from dawn to dusk. In the auroral zone are the flows reversed and the electric field $\mathbf{E}_a$ points in the opposite direction, from dusk to dawn. See Figure 2.6 for illustration.
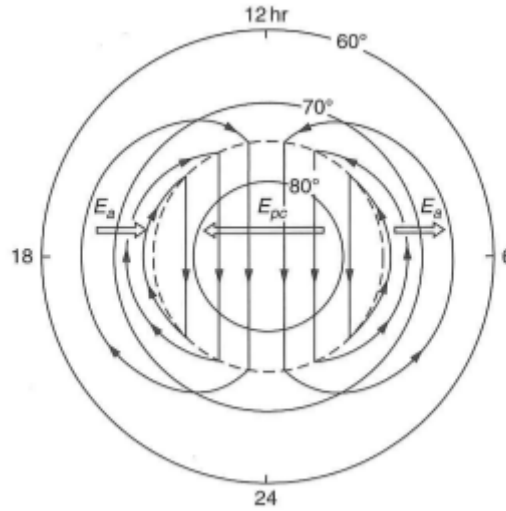
FIGURE 2.6: The solid contours indicates the plasma flow $\mathbf{v}$ and the arrows indicates the associated electric fields. Image credit: Kelly [34]

The ionosphere is an electrical conductive medium, and with the electric fields associated with the convection, a current is produced. These currents are discussed in section 2.6.

2.5.1 Field controversy

In the ionospheric research community it is debated whether flow is produced by the electric field or the other way around. This is called the $\mathbf{B}, \mathbf{v}$ vs $\mathbf{E}, \mathbf{j}$ controversy (Parker [53]). Proponents of the $\mathbf{E}, \mathbf{j}$ argues that the electric field and current are the primary variables while proponent of $\mathbf{B}, \mathbf{v}$ treats the magnetic field and plasma flow as the primary variables. Vasyliunas [70] argues that the sets of variables are equivalent for steady systems and only becomes important when time variations must be considered. He argues that the debate is resolved where the $\mathbf{B}, \mathbf{v}$ gives the correct physical understanding while $\mathbf{E}, \mathbf{j}$ is only a more mathematically convenient system. We agree that flow and magnetic field are the fundamental variables, but in this thesis we choose to describe ionospheric electrodynamics in terms of electric fields and currents.

2.6   Ionospheric Conductivity and Currents

The cycle of open and closed magnetic flux driven by the solar wind maps an electric field down to the ionosphere $\mathbf{E}_I$. Solar radiation and particle precipitation make the ionosphere an electrical conductive medium. A current is given by Ohm's law in the reference frame of the neutrals

$$\mathbf{j} = \boldsymbol{\sigma} \cdot \mathbf{E}_I \tag{2.3}$$

where $\boldsymbol{\sigma}$ is the conductivity tenor and we have neglected the term from the neutral wind. Kelly [34] expresses the conductivity tensor as

$$\boldsymbol{\sigma} = \begin{pmatrix} \sigma_P & -\sigma_H & 0 \\ \sigma_H & \sigma_P & 0 \\ 0 & 0 & \sigma_0 \end{pmatrix}$$

where σ_0, σ_H and σ_P is the *specific*, *Hall* and *Pedersen* conductivity respectively. The tensor elements are given by

$$\sigma_0 = ne(b_i - b_e) \tag{2.4}$$

$$\sigma_P = ne\left(\frac{b_i}{1 + \kappa_i^2} - \frac{b_e}{1 + k_e^2}\right) \tag{2.5}$$

$$\sigma_H = \frac{ne}{B}\left(\frac{\kappa_e^2}{1 + \kappa_e^2} - \frac{\kappa_i^2}{1 + \kappa_i^2}\right) \tag{2.6}$$

where $b_j = q_j/m_{gj}\nu_{jn}$ is the mobility and $\kappa_j = \omega_{gj}/\nu_{jn}$ is the gyro-frequency to collision frequency. The subscript j denotes i for ions and e for electrons. Taking the dot product of the conductivity tensor $\boldsymbol{\sigma}$ with the ionospheric electric field $\mathbf{E}_I$ we obtain the ionospheric current

$$\mathbf{j} = \sigma_0 \mathbf{E}_\parallel + \sigma_P \mathbf{E}_\perp - \sigma_H\left(\mathbf{E}_\perp \times \mathbf{B}\right)/B \tag{2.7}$$

where the subscripts indicates parallel and perpendicular to the terrestrial magnetic field. Hall and Pedersen conductivity governs *Hall currents* and *Pedersen currents* respectively. Pedersen currents flow parallel to the electric field and perpendicular to the magnetic field. Hall currents flows perpendicular to both the electric field and the magnetic field. We see can also see that Hall currents opposite to the convection flow. The specific

conductivity σ_0 is sometimes called *parallel conductivity* because the current flows parallel to the magnetic field (field-aligned currents). A figure of the field-aligned currents and horizontal Hall and Pedersen currents can be found in Figure 2.7.
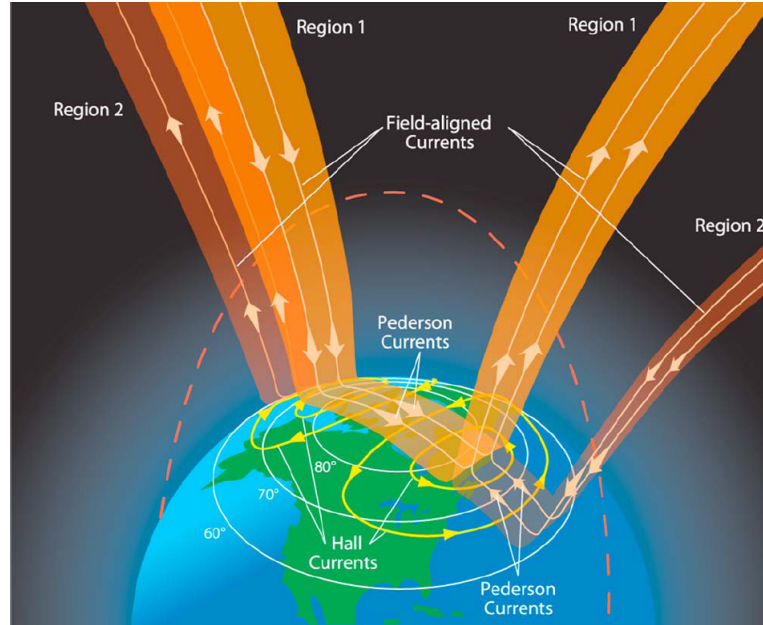
FIGURE 2.7: Schematic vies of Birkeland, Hall and Pedersen currents. Figure by Le et al. [45]

The absolute values of κ_i and κ_e determines the current system. There are three cases relevant at ionospheric heights:

- $|\kappa_i|$, $|\kappa_e| >> 1$:
  Neither electrons nor ions experience significant collisions and both undergoes E×B drift. All charged particles move in the same direction and no current is produced

- $|\kappa_i| \approx 1, |\kappa_e| >> 1$:
  The ions experience on average one collisions per gyration and the result is a net motion 45° angle to the electric field. Electrons on the other hand is in the collisionless case and moves perpendicular to the electric field. The result is a current parallel to the electric field i.e. Pedersen current

- $|\kappa_i| << 1, |\kappa_e| >> 1$:
  For the ions the collision frequency is so high that they have no net motion while electrons drifts nearly without collisions. This produces a current anti-parallel to the drift motion. This is in other words Hall current

The magnetic field lines at high latitudes are nearly vertical and the horizontal height-integrated current is given by

$$\mathbf{J}_\perp = \mathbf{J}_P + \mathbf{J}_H = \Sigma_P \mathbf{E}_\perp - \Sigma_H \left(\mathbf{E}_\perp \times \mathbf{B} \right) / B \tag{2.8}$$

where we have used the relations $\mathbf{J}_\perp = \int \mathbf{j}_\perp dz, \Sigma_H = \int \sigma_H dz, \Sigma_P = \int \sigma_P dz$ [4, p. 87]. The height-integrated conduction is also called conductance. Assuming current continuity it can be showed that field-aligned currents $j_\parallel$ is equal to

$$j_\parallel = \Sigma_P \left(\nabla_\perp \cdot \mathbf{E} \right) + \mathbf{E} \cdot \nabla_\perp \Sigma_P + \left(\mathbf{E} \times \nabla_\perp \Sigma_H \right) \cdot \hat{\mathbf{B}} \tag{2.9}$$

where $\hat{\mathbf{B}} = \mathbf{B}/B$. Field-aligned currents are also called *Birkeland currents*, named after the Norwegian scientist Kristian Birkeland who predicted the existence of these currents and linking them to the origin of aurorae (Birkeland [7, 8]). Birkeland's work these currents was mostly ignored by the scientific community until the existence was validated by the pioneering work by Iijima and Potemra [32].

Plasma flow and ionospheric currents are electrodynamic phenomena and are described by Maxwell's equations. When studying ionospheric electrodynamics it is convenient to apply some appropriate approximations of the equation set. At ionospheric heights are the largest perturbations in the magnetic field $\delta\mathbf{B}$ tiny compared to geomagnetic field $\mathbf{B}_{\text{geo}}$ ($\delta B/B_{\text{geo}} \leq 0.05$). Hence we only need to consider the geomagnetic field which we assume to be slowly varying and we can derive the electric field from a static potential ϕ

$$\mathbf{E} = -\nabla\phi \tag{2.10}$$

By inserting equation (2.10) in equation (2.8 and assuming that the magnetic field is perpendicular to the ground $\hat{\mathbf{B}} = \hat{z}$, where $\hat{z}$ is unit vector pointing upward, we can summarize $\mathbf{J}_H$ and $\mathbf{J}_P$ in the following way, according to Laundal et al. [43]:

Hall current

$$\mathbf{J}_H = -\Sigma_H \left(\nabla\phi \times \hat{\mathbf{z}} \right) \tag{2.11}$$

$$\nabla \cdot \mathbf{J}_H = - \left(\nabla\Sigma_H \times \nabla\phi \right) \cdot \hat{\mathbf{z}} \tag{2.12}$$

$$\nabla \times \mathbf{J}_H = \Sigma_H \nabla^2\phi \, \hat{\mathbf{z}} - \nabla\Sigma_H \left(\nabla\phi \times \hat{\mathbf{z}} \right) \tag{2.13}$$

and for Pedersen current

$$\mathbf{J}_P = -\Sigma_P \nabla \phi \tag{2.14}$$

$$\nabla \cdot \mathbf{J}_P = -\Sigma_P \nabla^2 \phi - \nabla \phi \cdot \nabla \Sigma_P \tag{2.15}$$

$$\nabla \times \mathbf{J}_P = -\nabla \Sigma_P \times \nabla \phi \tag{2.16}$$

2.7   Auroral Electrojets

At closed magnetic field lines particle can precipitate into the atmosphere and increase the conductivity of the ionosphere. This increased conductivity leads to powerful current in the auroral zone and hence the name *auroral electrojets*. The auroral electrojets consist of a eastward and westward electrojets flowing zonally. The electrojets are fed by downward Birkeland currents and increases in strength toward the midnight sector where. The eastward electrojet originate primarily in the dayside while half of the westward electrojet originates in the dayside. The westward electrojet covers most of the nightside from dawn to about 2000 MLT while the eastward electrojet is only present in the pre-midnight sector(Gjerloev and Hoffman [28]). These currents generates strong magnetic perturbations measurable on the ground which can exceed over $1000nT$. *The auroral electrojet indices*(Davis and Sugiura [16]) have been developed to give and indication of the electrojet activity. These indices are derived from magnetometer stations placed in the auroral zone in NH. This is discussed further in section 3.3.
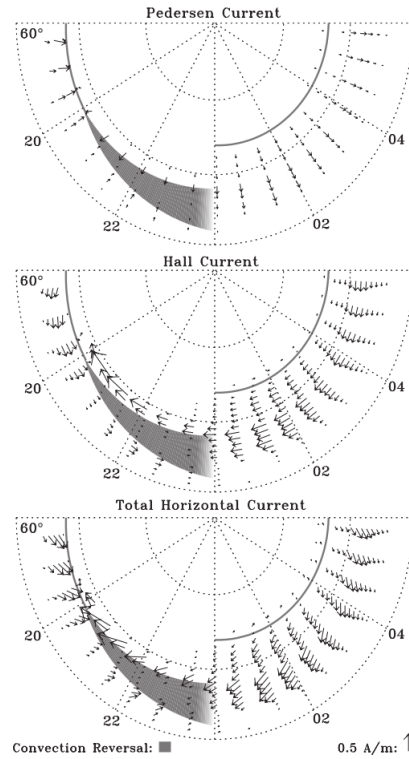
FIGURE 2.8: Horizontal current pattern in the ionosphere.
Figure by Gjerloev and Hoffman [28]

The auroral zone is composed of a narrow band of high conductivity, much higher than that of the polar cap. Therefore, currents flow much more easily in this region. The horizontal current patterns in the nightside ionosphere is shown in Figure 2.8. The electric field associated with the plasma convection experiences a sharp turn in the pre-midnight sector referred to as the *Harang discontinuity region* (Harang [29], Koskinen and Pulkldnen [38], Kunkel et al. [39]). There is a drop of current density in this region. This is indicated as the shaded area in Figure 2.8.

The strongest electrojets occurs during *magnetospheric substorms*. These substorms results from an imbalance between the dayside and nightside reconnection rate causing an excess of magnetic flux being transported from the dayside over to the magnetotail. Magnetic flux is being stored in the tail lobes and when reconnection eventually occurs, magnetic energy is ejected and transmitted down to the ionosphere. This results in increased electrojets and visible aurorae (Akasofu [1], Kisabeth and Rostoker [36], Rostoker [60]).

2.8 Measuring Magnetic Perturbations

A current $\mathbf{j}$ is related to a magnetic field $\mathbf{B}$ by Amperes law

$$\nabla \times \mathbf{B} = \mu_0 \mathbf{j} \tag{2.17}$$

where μ_0 is *the magnetic permeability of free space.* For steady currents the magnetic field $\mathbf{B}$ in equation 2.17 can be expressed on integral form, commonly known as *Biot-Savart law*

$$\mathbf{B}(\mathbf{r}) = \frac{\mu_0}{4\pi} \int \frac{\mathbf{j}(\mathbf{r}') \times \mathbf{R}}{\mathbf{R}^3} d\tau \tag{2.18}$$

where $\mathbf{R} = \mathbf{r} - \mathbf{r}'$ is the separation vector, r is the field point (where the field is calculated from), r' is the source point (where the currents are) and $d\tau$ is the volume element. We have now established the relevant field equations for ionospheric electrodynamics, however calculating them from ground based magnetic perturbation data is not straightforward; the curl in 2.17 is unknown and cannot be used to determine the current. Vasyliunas [69] showed that Biot-Savart integral over regions with radial magnetic field lines is zero expect for divergence horizontal divergence-free currents. This result is known as the *Fukushima theorem* (section 2.9) and is used in the definition of equivalent currents (section 2.10).

2.9 Fukushima Theorem

The Fukushima Theorem is a central theorem in ground based geomagnetic studies. Fukushima [23, 24, 25] demonstrated that for magnetic field lines perpendicular to the ground, magnetic perturbation produced by field-aligned current and horizontal divergent current will cancel each other. An observer on the ground will therefore not register any magnetic perturbations from the ionosphere as shown in Figure 2.9. This theorem is relevant at high latitudes where the magnetic field lies are nearly perpendicular to the ground.

From the Fukushima theorem and equations (2.13) and (2.16) it can be shown that magnetic perturbations measured on the ground is mainly produced by Hall currents. If the horizontal ionospheric conductivity gradients are zero $\nabla \Sigma_H = \nabla \Sigma_P = 0$ then it follows that $\nabla \cdot \mathbf{J}_H = 0$ and $\nabla \cdot \mathbf{J}_P \neq 0$. Only divergence free currents produces measurable magnetic perturbations which we just showed were Hall currents. The
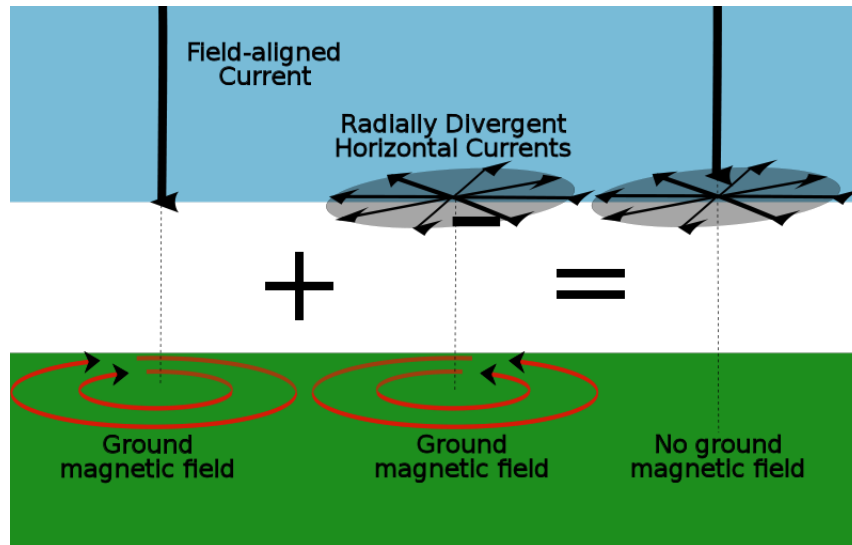
FIGURE 2.9: Birkeland currents and radially divergent horizontal currents cancels each other and no magnetic perturbations are registered on the ground. https://upload.wikimedia.org/wikipedia/en/2/20/Fukushima-cancelation.svg

Fukushima theorem is essential in the concept of *equivalent currents* discussed in section 2.10. Untiedt and Baumjohann [67] showed that the Fukushima theorem is a good approximation if $\sin I$ is close to unity where I is the magnetic inclination.

2.10 Equivalent Currents

For decades researchers have used ground based magnetometers for study of ionospheric electrodynamics. Horizontal ionospheric currents induce magnetic perturbations that are measurable on the ground, however, reconstruction of true horizontal ionospheric currents from magnetic perturbation is not a trivial task. Instead, researchers have introduced the concept of *equivalent currents*. Equivalent currents are the horizontal current at some height which would produce the observed perturbations by ground magnetometers. Friis-Christensen et al. [21] used a chain of ground magnetometers along the coast of Greenland to produce a global map of the equivalent current system in NH. Laundal et al. [44] made a similar map where the effect of sunlight is included. The map is showed in 2.10.
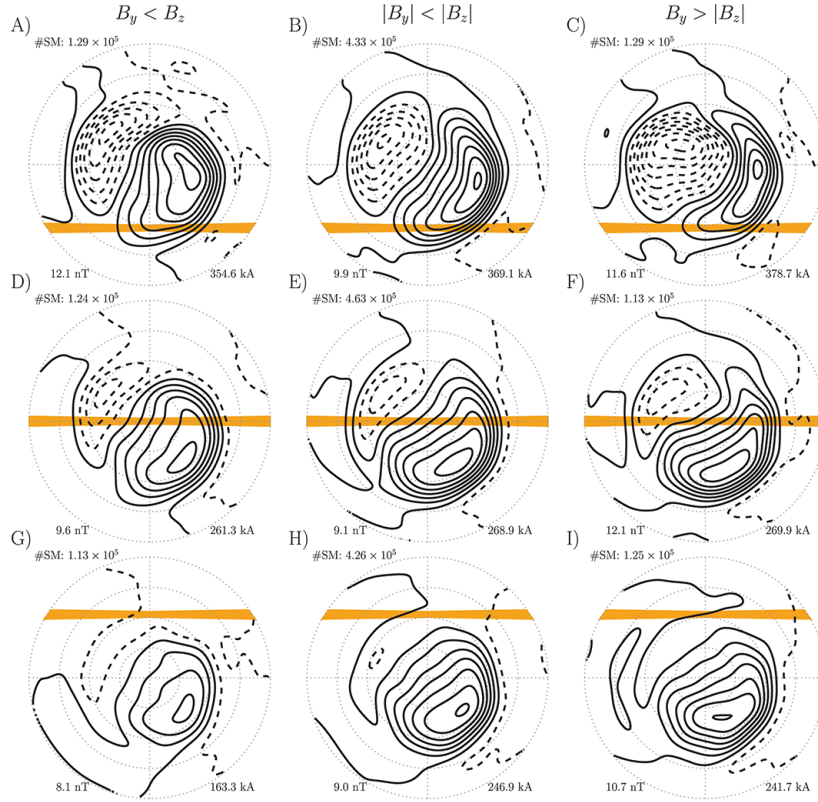
FIGURE 2.10: Equivalent currents system at different IMF configurations. The yellow lines indicate the sunlight terminator. The column on the left [A), D), G)] indicates negative IMF B_y, the column in the middle [B), E), H)]indicates neutral IMF B_y and the column on the right [C), F), I)] indicates positive IMF B_y. The black contours indicate equivalent current flow. Solid contours mean anti-clockwise flow and dashed contours mean clockwise flow. Figure by Laundal et al. [44]

Maps by Friis-Christensen et al. [21] and Laundal et al. [44] reveal some important features of the equivalent currents system, such as the two-cell circulation pattern and the electrojets. Laundal et al. [44] found that in the sunlit ionosphere the equivalent current system is similar to Hall currents, but the equivalent current system indirectly affected by Birkeland currents in darkness.

2.10.1 Definition of Equivalent Currents

A current $\mathbf{J}$ flowing in the ionospheric layers can be decomposed into a field-aligned current and a height-integrated horizontal current $\mathbf{J} = \mathbf{J}_{\parallel} + \mathbf{J}_{\perp}$. Furthermore, the horizontal part can be decomposed into a divergence-free part and a curl-free part, $\mathbf{J}_{\perp} = \mathbf{J}_{\perp,\mathrm{df}} + \mathbf{J}_{\perp,\mathrm{cf}}$ according to Helmholtz theorem. According to the Fukushima theorem (section 2.9) only divergence-free currents can be registered and hence we can set the equivalent current equal to the divergence-free current, $\mathbf{J}_{\mathrm{eq}} = \mathbf{J}_{\perp,\mathrm{df}}$. It is important to note that equivalent currents are mathematical constructions and not physical currents. Equivalent currents

can be related to real ionospheric currents e.g. if the ionospheric conductivity is uniforms it can be showed that the equivalent current is equal to Hall current (see section 2.9).

2.10.2 Sunlight impact on Equivalent Currents

Studies by Laundal et al. [43, 44] demonstrated that the main contribution to the equivalent current system is different for the sunlit and dark ionosphere. They found that in Hall currents dominates in the sunlit ionosphere and Birkeland currents influence the current system indirectly in the dark ionosphere. This was shown by how $\mathbf{J}_\perp$ is decomposed into divergence-free and curl-free components. They argue that for a flat geometry ionosphere the curl-free component can expressed as a gradient of a scalar potential $\mathbf{J}_{\perp,\mathrm{cf}} = \nabla_\perp \alpha$. The divergence of this current is given by

$$\nabla \cdot \mathbf{J}_\perp = \nabla_\perp^2 \alpha = -J_\parallel \tag{2.19}$$

which can be solved for α by the Green function for the two-dimensional Laplacian. The result is given by

$$\alpha(\mathbf{r}_\perp) = -\frac{1}{2\pi} \int \ln |r_\perp - r'_\perp| J_\parallel(\mathbf{r}'_\perp) \mathrm{d}\mathbf{r}'_\perp \tag{2.20}$$

Finally,they expressed the equivalent current system in the following way

$$\mathbf{J}_{\mathrm{eq}} = \mathbf{J}_{\perp,\mathrm{df}} = \mathbf{J}_\perp - \mathbf{J}_{\perp,\mathrm{cf}} = \mathbf{J}_\perp - \nabla_\perp \alpha(\mathbf{r}') \tag{2.21}$$

If the horizontal current system $\mathbf{J}_\perp$ is zero then equation 2.21 reduced to $\mathbf{J}_{\mathrm{eq}} = -\nabla_\perp \alpha(\mathbf{r}')$ and the equivalent current system is completely determined by the Birkeland current system. In the dark polar cap the horizontal current is probably very small which makes this area a suitable testing ground. This was tested by Laundal et al. [43] by numerical calculations of $-\nabla_\perp \alpha$ and with data from *Active Magnetosphere and Planetary Electrodynamics Responds Experiment* (AMPERE). This current is sometimes called *fictitious horizontal closure currents* (Untiedt and Baumjohann [67]).Equivalent currents were approximated as as $\Delta \mathbf{B}_{gnd} \times \hat{\mathbf{z}}$ where $\Delta \mathbf{B}_{gnd}$ is magnetic perturbations measured on the ground using SuperMAG data and $\hat{\mathbf{z}}$ is the unit vector point upward. Their result is shown in Figure 2.11.
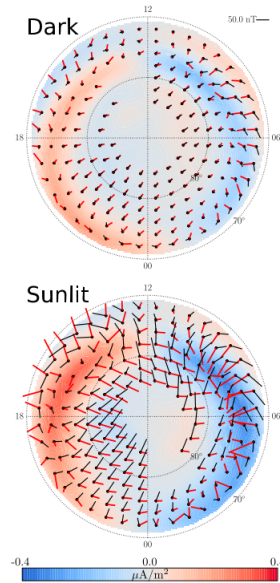
FIGURE 2.11: The background color indicates the intensity of the Birkeland current system, black vectors are equivalent currents $\Delta\mathbf{B}_{gnd} \times \hat{\mathbf{z}}$ and red vectors are $-\nabla_\perp\alpha$. Figure by Laundal et al. [43]

Laundal et al. [43] considered two extreme cases and interpreted their physical meaning.

- $\Sigma_H = \Sigma_P = 0$ (locally):

  If there are no conductance in ionosphere then there are no horizontal currents and the equivalent current system would be completely determined by Birkeland currents $\mathbf{J}_{\text{eq}} = -\nabla_\perp\alpha$.

- $\nabla\Sigma_H \cdot \mathbf{v} = \nabla\Sigma_P \cdot \mathbf{v} = 0$ (globally):

  If the ionospheric convection flow $\mathbf{v}$ is perpendicular to both Hall and Pedersen gradients then it can be showed that the equivalent current system is perpendicular to $-\nabla_\perp\alpha$ and anti-parallel to the equivalent current system. In other word we can set $\mathbf{J}_P = \nabla_\perp\alpha$ and $\mathbf{J}_{\text{eq}} = \mathbf{J}_H$.

Birkeland current is related differently to ground magnetic perturbations in darkness and sunlight. Laundal et al. [43] interpreted the result in 2.11 as such; in darkness currents in the polar cap is very small and equivalent currents are indirectly related to Birkeland currents in the polar cap. In sunlight the polar cap is more conducting and Hall currents dominates. Birkeland currents are not registered by the ground magnetometers.

2.11   Sunlight Terminator

The main source of ionization on the dayside is photoionization and particle precipitation in the sunlit ionosphere. Ionization by particle precipitation is very complex and it is hard to determine ionospheric conductivity for ionosphere in darkness. On the other hand several empirical models relating Hall and Pedersen conductances to the solar zenith angel χ and the 10.7 cm solar flux S_a. Most of such empirical models indicates that the ionospheric conductance is scaled as $\cos^{0.5}\chi$ (Moen and Brekke [49], Robinson and Vondrak [58], Vickrey et al. [71]). The Hall and Pedersen conductance reported by Moen and Brekke [49] are given in equations (2.23) and (2.23) respectively. These equations are plotted as a function of χ are shown in Figure 2.12a.

$$\Sigma_H = S_a^{0.53}\left(0.81\cos\chi + 0.54\sqrt{\cos\chi}\right) \tag{2.22}$$

$$\Sigma_P = S_a^{0.49}\left(0.34\cos\chi + 0.93\sqrt{\cos\chi}\right) \tag{2.23}$$

The sunlight terminator has been defined as the contour of $\chi = 90°$ (e.g. Laundal et al. [44], Moen and Brekke [49]) where the sunlit ionosphere is below this solar zenith angle and conductances are scaled as $\cos^{0.5}\chi$ and ionization by particle precipitation is dominant at the nightside. However, this leads to some complications due to the fact that the conductance gradients are infinite at the terminator. This is illustrated in Figure 2.12b.
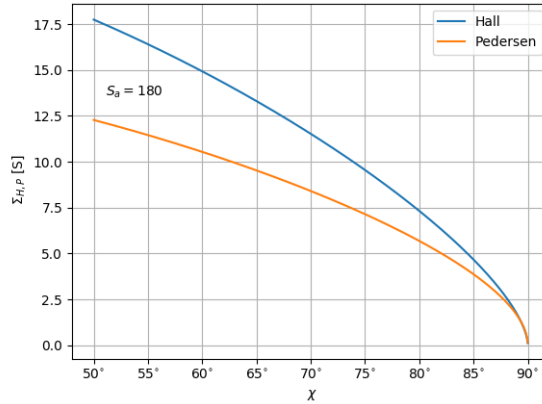
(A) Hall and Pedersen conductances by Moen and Brekke [49] evaluated at $S_a = 180$
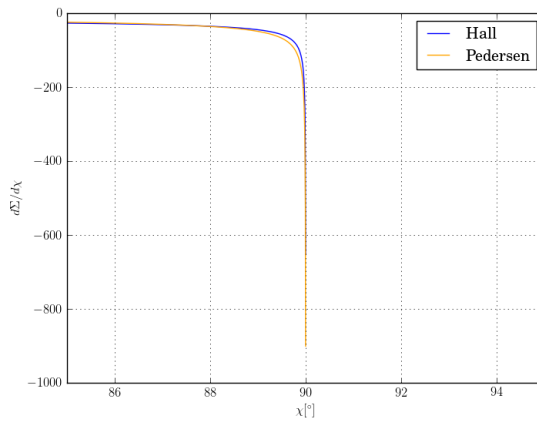
(B) Gradients in conductances (2.23) and (2.23) approaches infinity at the daytime terminator.

From equation (2.9) we can see that infinite conductance gradients leads to infinite Birkeland currents. Also, from equations (2.13) and (2.16) it follows that the horizontal currents would have infinite curl and divergence. This implies that charge density builds up indefinitely fast. These attributes are physically impossible and alternative values of χ should therefore be considered.

2.12 Magnetic Field Asymmetries

Ionospheric currents are proportional to the electric conductivity and from equations (2.6) and (2.5) we can see that the conductivity elements are dependent on the ratio of gyro-frequency ω_g to collision frequency ν. The gyro-frequency is given by $\omega_g = qB/m$ which suggest that ionospheric currents at a given point are affected by the strength of the ambient magnetic field $\mathbf{B}$. The geomagnetic field is neither uniform nor symmetric,

hence the magnetic field strength at magnetic conjugate points differs. The asymmetries in the Earth's magnetic field is shown in Figure 2.12.
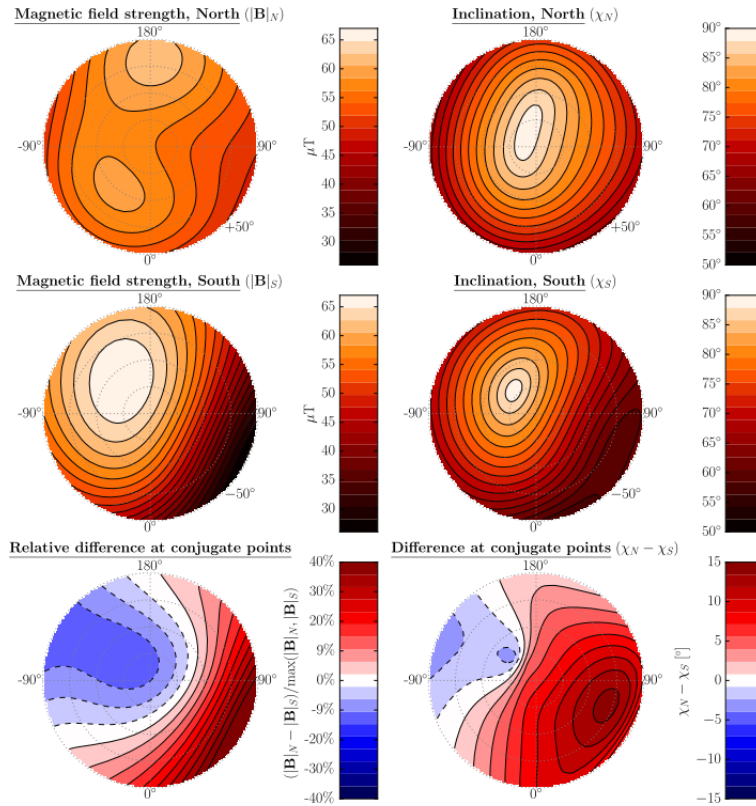
FIGURE 2.12: The column at the left displays magnetic field strength for NH *(top)* , SH *(middle)* and inter-hemispheric difference *(bottom)*. At the right column we have the magnetic inclination. Calculations was performed by the IGRF-12 model evaluated at $1R_E$ and using 2015 coefficients. Figure by Laundal and Richmond [42]

From equations (2.8) and (2.9) we find that the currents are given by the magnetic field **B** and the conductance, which is height-integrated conductivity. This implies that the size of the ionospheric current is a function of the magnetic field strength B. Richmond [57] and Cnossen et al. [12] reported that the horizontal ionospheric conductances are scaled with the magnetic field strength. Richmond [57] found that Hall and Pedersen conductances are scaled as $B^{-1.3}$ and $B^{-1.6}$ respectively. Cnossen et al. [12] found higher dependency. Their findings were $B^{-1.7}$ for Hall conductance and $B^{-1.5}$ for Pedersen conductance. A plot of conductances scaled according to values reported by Richmond [57] is shown in Figure 2.13.
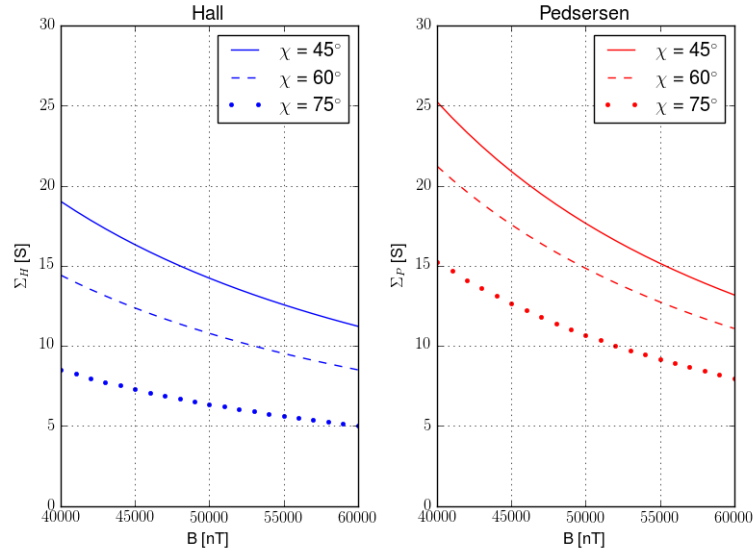
FIGURE 2.13: Hall conductance Σ_H (left) and Pedersen conductance Σ_P (right) are according to Richmond [57] scaled as $B^{-1.3}$ and $B^{-1.6}$ respectively. In this figure we have evaluated conductances with solar activity level $S_a = 180$

2.13   IMF By asymmetries

Several asymmetric feature are associated with the IMF B_y component. The ionospheric convection pattern is distorted (Cowley [13], Heppner [30], aurora onset location is longitudinal displaced between the hemispheres (Liou and Newell [46], Østgaard et al. [50, 51]) and changing the morphology of the equivalent currents pattern (Friis-Christensen et al. [21], Laundal and Richmond [42]).
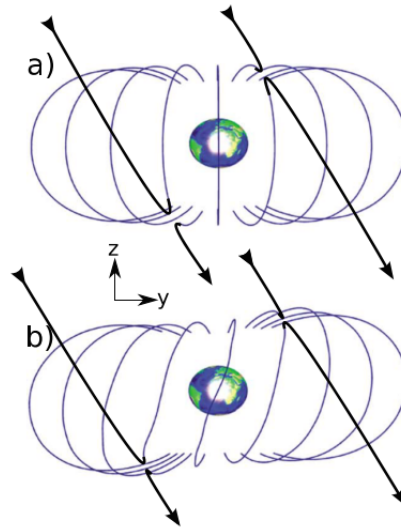
FIGURE 2.14: a) The IMF (black lines) reconnects with the geomagnetic field lines (blue lines) produces magnetic field lines convecting towards dusk and dawn by magnetic tension. b) Induced B_y on closed field lines alters the reconnection geometry. Figure adapted from Tenfjord et al. [65]

2.13.1 Asymmetric ionospheric convection patterns

When the IMF B_y is present the dayside reconnection site is moved from the subsolar point and towards the high latitude flanks. The newly reconnected magnetic field line has a great curvature which give rice to magnetic tension $\vec{\mathbf{T}}$ acting to straighten out the magnetic field line. The tension on the newly open field line is transmitted down the ionosphere and the associated Lorentz-force accelerates the ionospheric plasma on the dayside (red vector in Figure 2.15) in the direction by the imposing forces. The shift of the dayside reconnection region also lead to asymmetric distribution of magnetic flux in the magnetosspheric tail lobes. This accumulation of magnetic flux leads to an increase of magnetic pressure ∇P_{mag} which acts to balance the magnetic tension force on the nightside. The pressure force, from plasma pressure and magnetic pressure, ∇P_0 leads to the characteristic rounded and crescent shaped ionospheric convection cells. The convection patterns are close to mirror images of each other in the hemispheres (Cowley [13]).
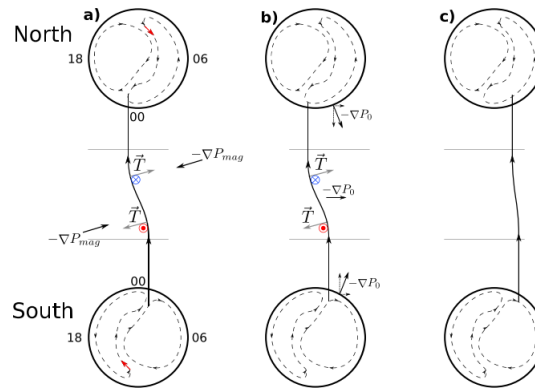
FIGURE 2.15: Tension $\vec{\mathbf{T}}$ and magnetic pressure force ∇P_{mag} determines the direction of the plasma flow and hence the morphology of the ionospheric convection pattern. Figure adapted from Tenfjord et al. [65]

2.13.2 Asymmetric foot points of magnetic field lines

The IMF B_y can alter the geometry of the closed magnetic field lines and cause asymmetric foot points of the magnetic field lines. When the IMF has an B_y component the magnetic field on the dayside is twisted as shown in Figure 2.14. The foot points of the open magnetic flux are tied to the plasma convection as discussed in the previous section. Magnetic stress moves the magnetic field lines (Tenfjord et al. [65]). The closed magnetic field lines are now twisted as illustrated in Figure 2.14 b). The twisting of magnetic field lines are linked to asymmetric auroral features between the hemispheres.

Charged particles are tied to the magnetic field lines and bounces back and forth between the mirror point in the hemispheres. This is called *bounce motion* and results from the first adiabatic invariant. The first adiabatic invariant states that the magnetic moment μ of a charged particle under the influence of electromagnetic forces is conserved. It can be showed that the magnetic moment is equal to

$$\mu = \frac{mv^2 \sin^2 \alpha}{2B} \tag{2.24}$$

where m and v is the particles mass and velocity respectively and α is the pitch angle. As the particle moves along field lines towards the Earth they will eventually reach a point where the pitch angle is equal to 90° and the particles are reflected back by the so-called *mirror force* $F_m = -\mu \nabla_\parallel B$. The points where the particle is reflected back is called the mirror point. In a symmetric magnetic field, like the dipole field, particles bounces between the mirror points along the magnetic field lines. Not all particle are able to escape back to the magnetosphere though; if the mirror point lies too deep in the atmosphere the particles will precipitate into the atmosphere. It can be showed that the pitch angle at the equatorial point α_{eq} is given by

$$\sin^2 \alpha_{eq} = B_{eq}/B_m \tag{2.25}$$

where B_{eq} is the magnetic field strength at the equatorial plane and B_m is the magnetic field strength at the mirror point. If this angle is less than α_l then will the particle precipitate into the atmosphere. Energetic precipitation in the atmosphere can ionize the ionosphere, leading to strong horizontal currents, and create bright aurorae.

If the magnetic field were symmetric we would expect conjugate aurora. However many non-conjugate auroral phenomena has been reported. Østgaard et al. [50] studied simultaneous aurora images and hemispherical asymmetry in the auroral features.

A follow-up study by Østgaard et al. [51] found that the longitudinal displacement of the auroral features were strongly correlated with the IMF B_y and derived an empirical formula given by

$$\Delta\text{MLT} = 0.88 \times \sin\left(\frac{B_y}{12nT} \times 90° - 9.3°\right) \tag{2.26}$$

where $\Delta\text{MLT} = \text{MLT}_{SH} - \text{MLT}_{NH}$.
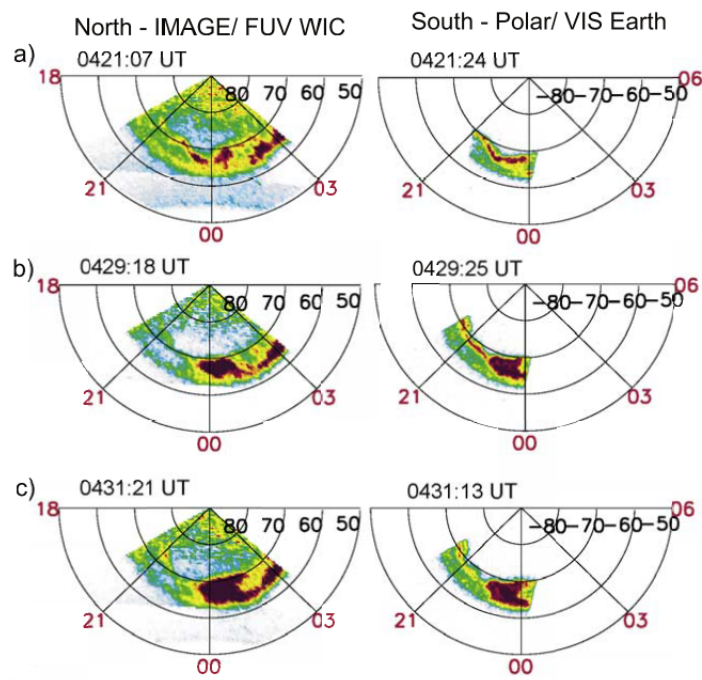
FIGURE 2.16: Images of the conjugate hemispheres during the 2 July 2001 substorm. Figure adapted from Østgaard et al. [50]

Chapter 3

Instruments and Data

Magnetic perturbation data are made available by the *SuperMAG*-collaboration which provides magnetometer data from both hemispheres. The data are stored in a common reference system with 1-minute resolution. The equivalent current system is dependent on the orientation of the IMF, hence the necessity for solar wind data. The solar wind and inter planetary magentic field (IMF) measurements are provided by the ACE, Wind, IMP-8 and Geotail satellite and are downloaded from the OMNIWeb database at `https://omniweb.gsfc.nasa.gov/`.

3.1   SuperMAG

The magnetometer data are provided by SuperMAG. SuperMAG is a collaborating which provides global monitoring of terrestrial magnetic field. There exists many difficulties associated with geomagnetic measurements since providers of magnetometers data may utilized different magnetic coordinate systems and time resolutions and the baseline may or may not be removed. In order to overcome these problems SuperMAG data are rotated in a common coordinate system with 1-min time resolution and the baseline has been removed. This data process is described by Gjerloev [27]. Magnetometer data are downloadable for free and can be found in the link `http://supermag.jhuapl.edu`. As of 2017 more than 400 stations are available. A map of SuperMAG stations is given in Figure 3.1.

SuperMAG provides magnetic perturbation vectors in the NEZ-coordinate system. In NEZ-coordinates the magnetic field vectors is given by $\mathbf{B} = (B_N, B_E, B_Z)$ where B_N is in local magnetic north, B_E is local magnetic east and B_Z is vertically down. The rotation is based on a time-dependent declination determined by
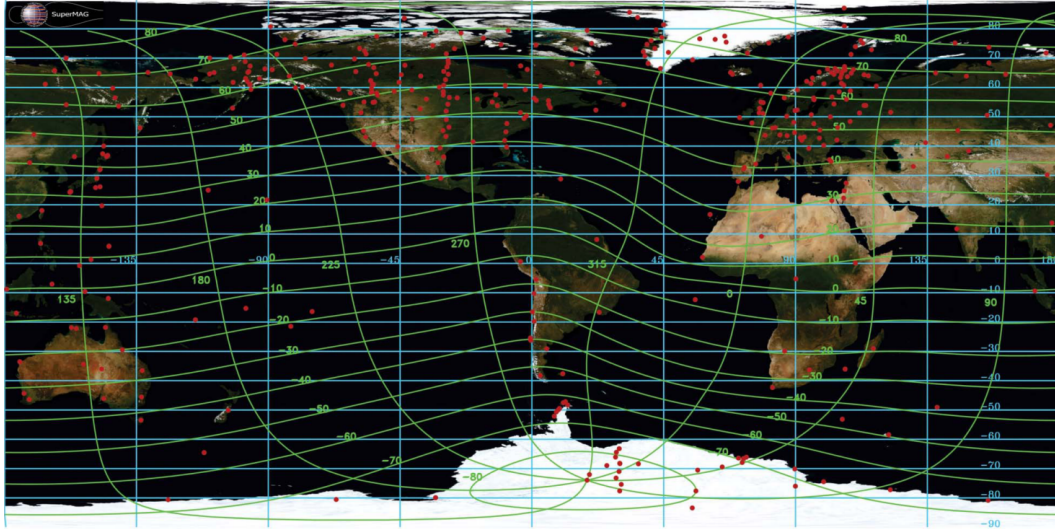
FIGURE 3.1: Red dots are locations of SuperMAG stations. Geographic coordinates are showed in cyan and magnetic coordinates are showed in green. This maps shows the global coverage of ground magnetic field measurements. Map provided by Gjerloev [27]

$$\theta(t) = \arctan(B_{1,\perp}(t)/B_{2,\perp}(t)) \tag{3.1}$$

where $B_{i,\perp}$ is the ith component in the field.

The baseline determination technique is based on 1) identity and remove the daily trend, 2) identity and remove the yearly trend and 3) remove any remaining offset. This process is designed such that only magnetic perturbations produced by currents in the ionosphere is maintained [1] and leave out other sources. The process is validated by Gjerloev [27] and described in more details below.

---

[1] S_q currents are also ionospheric current, but the SuperMAG processing technique are design to remove these currents as well

SuperMAG Dataflow

Data From Collaborator
- time resolution: anything
- coordinate system: anything
- baseline: included or removed
- errors and artifacts: included
- format: anything

Initial Data
- time resolution: 1-min
- coordinate system: anything
- baseline: included or removed
- errors and artifacts: included
- format: binary (IDL save files)

Data Cleaning
Automated and manual error identification. Errors and their solutions are saved in ascii file.

Rotated Data
- time resolution: 1-min
- coordinate system: NEZ
- baseline: included or removed
- errors and artifacts: removed
- format: binary (IDL save files)

Final Data
- time resolution: 1-min
- coordinate system: NEZ
- baseline: removed
- errors and artifacts: removed
- format: binary (IDL save files)

FIGURE 3.2: This figure gives an illustration of the steps involved in the SuperMAG data processing. Figure from Gjerloev [27]

3.1.1 Daily trend

The first step involves rotating the raw data into the NEZ coordiante system using the declination defined in equation (3.1). A slowly varying trend in the rotated data is determined from a 1 day window. The trend is determined from a typical value for each day and then resampled from 24 h resolution to 1 min resolution format. The diurnal variations are determined by the residuals of the rotated data and the daily trend from 3 days (a given day and the neighbouring days). A typical value for each 30 min interval is found yields 48 data points for each day. The daily trend is then found by a weighed fit and resampling of these semi-hourly values.

3.1.2 Yearly trend

The determination of the yearly trend is based on typical values within 17 day sliding window. For each day a typical value is determined where the daily trend has been removed. The yearly trend is then found by smoothing and resampling these values using an appropriate method.

3.1.3 Residual offset

Residual offset is based probability distribution of official quiet days. It is assumed that typical values during quiet days are zero and any residual offset are removed from the dataset.

3.2 OMNIWeb

Equivalent current system is greatly affected by the orientation of the IMF (e.g. Friis-Christensen et al. [21], Laundal and Richmond [42]). Solar wind and IMF data are made available from OMNIWeb database provided by NASA and downloadable from `https://omniweb.gsfc.nasa.gov/ow_min.html`. Measurements are made by the spacecraft ACE, IMP-8, Wind and Geotail which carries magnetometer instruments. As the spacecraft orbits the Earth they make measurements at different locations along the orbit which may be several Earth radii away from the Earth-Sun line. Therefore, the data have been time shifted from their location of observation to a common point, chosen to be the bow shock nose. This time shift is performed by a procedure developed by Weimer et al. [73] which is based on a assumption that the IMF values measured by the spacecraft at a given time and location lie on a planar surface called the *phase font*. It is further assumed that the same values would be measured at a different time and location when the phase font sweeps to this place. In order to calculate the time shift a bow shock model given by Farris and Russell [19] and magnetopause model by Shue et al. [62] is used. The fluctuations in the IMF may be tilted with respect to the Sun-Earth line which causes the IMF to propagate in an other direction than expected. Determination of this tilt angle can be performed by *minimum variance analysis* (MVA) technique (e.g. Weimer et al. [74]).

3.3 Auroral Electrojet Indices

Davis and Sugiura [16] defined indices designed to provide numerical measure of magnetic activity produced by ionospheric currents within in the aurora oval. The data are derived from 12 magnetometer stations located along the northern auroral zone in different time zones. Observations are based on readings of the horizontal component H of the magnetic field. The AL-index is defined as the lowest normalized H value measured by all the stations within 1-min. The AU-index is the highest registered value. The AL-index indicates the strongest intensity of the auroral westward electrojets while the AU-index indicates the strongest eastward auroral electrojet. The AE-index is intended

to be a measure of the global electrojet activity and defined as the difference between AU and AL, i.e. $AE = AU - AL$. Another index, the AO is defined as the average of AL and AU, $AO = (AU + AL)/2$ and gives a measure of the equivalent zonal current. These indices are used extensively for substorm and space weather studies. Since these indices are quantitative, they are very suitable for computer processing techniques and statistical studies.

As mention above magnetic activity from auroral electrojets are only covered in the northern hemishere and conjugacy between hemispheres has previously been assumed. However Weygand et al. [75] developed equivalent AE-index for southern hemisphere. In many cases, there were good agreement between these indices with a correlation coefficient above 0.7. However, in some intervals there correlation was close to zero. The mean difference between northern and southern AE was largest during IMF $B_z < 0$ and large $|\text{IMF}B_y|$ values. Some caution is recommended for analysis of southern electrojets by using the standard AE-index.

Some authors disagree with the interpretation of the derived AE and AO indices. Lutjeharms et al. [47] argue that these indices have no real physical meaning and should not be used in scientific studies. According to these authors the problem arises from the fact that the behaviour of AL and AU can be quite different and a summation (or subtraction) of the indices does not have a clear interpretation. They therefore suggest using AL and AU separately.

Chapter 4

Data Processing and Methodology

Ionospheric currents are associated with solar wind - magnetosphere interaction processes which takes place at high altitudes and are highly organized by how the Earth's magnetic field is mapped from these altitudes to the ionosphere. Therefore we need a coordinate system which takes this mapping into account. Several coordinate systems have been proposed, each designed for different purposes and regions. The Quasi-Dipole (QD) coordinate system (Richmond [56]) is suitable for horizontal ionospheric currents, equivalent currents and magnetic perturbations on ground level. This coordinate system is a modification of the Apex coordinate system (Vanzandt et al. [68]) defined by tracing of magnetic field lines. The magnetic field deviates significantly from a dipole field at ionospheric heights hence we have used the more realistic *International Geomagnetic Reference Field* (IGRF) (Thébault et al. [66]) as a model of the Earth's magnetic field.

Magnetic perturbation data provided by SuperMAG (Gjerloev [27]) are given in the NEZ components which is less suitable for ionospheric research than QD coordinates (Laundal and Gjerloev [41]) so we have converted the NEZ-coordinates into QD coordiatens. This conversion process involves two steps. First rotating NEZ components into geographic components using the IGRF declination and then converting geographic components into QD components using the computer software developed by Emmert et al. [18]. This process is explained more in the following sections.

4.0.1 International Geomagnetic Reference Field

The International Geomagnetic Reference Field (IGRF) is a standard mathematical model of the Earth's internal magnetic field [66]. The internal magnetic field **B** is described as a gradient of a scalar magnetic potential by $B = -\nabla V$ where V is the magnetic potential given in terms of a truncated series of spherical harmonics

$$V(r, \theta, \varphi, t) = a \sum_{n=1}^{N} \sum_{m=0}^{n} \left(\frac{a}{r}\right)^{n+1} [g_n^m(t) \cos(m\varphi) + h_n^m(t) \sin(m\varphi)] P_n^m(\cos\theta) \quad (4.1)$$

where r is the radial distance from the Earth, a is the geomagnetic conventional mean reference spherical radius of the Earth and is set equal to 6371.2 km, θ geocentric co-latitude and φ denotes longitude. $P_n^m(\cos\theta)$ are Schmidt semi-normalized associated Legendre functions of degree n and order m. g_n^m and h_n^m are Gaussian coefficients of the internal magnetic field. The magnetic field of the Earth is constantly changing and the IGRF model is for this reason updated every five years. In order to find coefficients between model periods, linear interpolation between the closest periods is used. The latest IGRF models uses truncation level N=13 so 195 Gaussian coefficients in equation (4.1) must be determined. Computation of the coefficients is based of data from global ground magnetometer and satellite observations. The latest version is the 12th generation downloadable from the link `https://www.ngdc.noaa.gov/IAGA/vmod/igrf.html`.
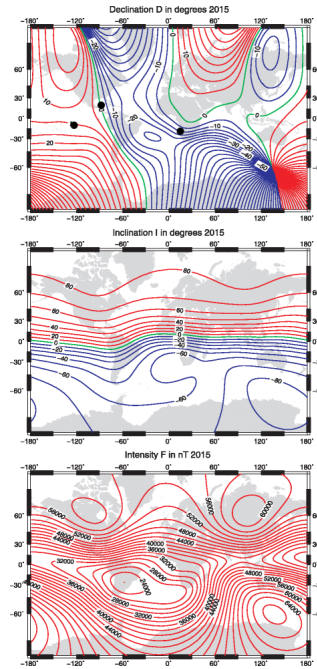
FIGURE 4.1: Map of the declination D (top), inclination I (middle) and intensity F (bottom) at the Earth's mean radius. Units of D and I are in degrees and the unit of the intensity F is in nT. Figure by Thébault et al. [66]

The geocentric components of the magnetic field. north (X), east (Y) and radially inwards (Z), are given by the magnetic potential V

$$X = \frac{1}{r}\frac{\partial V}{\partial \theta} \tag{4.2}$$

$$Y = -\frac{1}{r\sin\theta}\frac{\partial V}{\partial \varphi} \tag{4.3}$$

$$Z = \frac{\partial V}{\partial r} \tag{4.4}$$

The total intensity F, horizontal intensity H, declination D and inclination I are calculated from the components defined above.

$$F = \sqrt{X^2 + Y^2 + Z^2} \tag{4.5}$$

$$H = \sqrt{X^2 + Y^2} \tag{4.6}$$

$$D = \arctan(Y/X) \tag{4.7}$$

$$I = \arctan(Z/H) \tag{4.8}$$

Declination, inclination and total intensity from the IGRF-12 is plotted in Figure 4.1 for the year 2015.

4.0.2 Magnetic Apex Coordinate System

The Magnetic Apex coordinate system (Vanzandt et al. [68]) is defined in terms of a apex height h_a which is found by tracing the IGRF magnetic field line from a point in question to the highest point above the surface of the Earth. The Earth is modelled as a geoid, taking the ellipsoidal shape of the Earth into account. See Figure 4.2 for illustration.
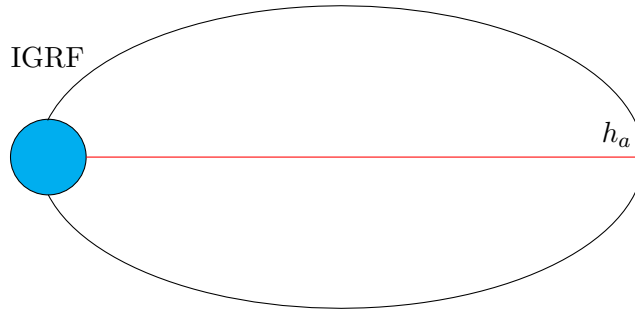
FIGURE 4.2: Apex definition

When the apex height h_a has been found then the magnetic apex coordinate can be calculated. The apex latitude λ_a is given by

$$\lambda_a = \pm \arccos \sqrt{\frac{R_{eq}}{R_{eq} + h_a}} \tag{4.9}$$

The plus-minus sign indicates positive values for the northern hemisphere and negative values for the southern hemisphere. The other apex coordinate is the apex longitude which is defined as

$$\varphi_a = \arcsin \left[\frac{\cos \lambda \sin(\varphi - \varphi_0)}{\cos \lambda_D} \right] \tag{4.10}$$

Here λ and φ are geographic latitude and longitude respectively and λ_0 and φ_0 are the coordinates of the north pole of the geomagnetic dipole field. λ_D is the dipole latitude and is given by

$$\lambda_D = \arcsin \left[\sin \lambda \sin \lambda_0 + \cos \lambda \cos \lambda_0 \cos(\varphi - \varphi_0) \right] \tag{4.11}$$

4.0.3 Quasi-Dipole Coordinate System

The Quasi-Dipole Coordinate System (QD) is modification of the Apex Coordinate System and is developed by Richmond [57]. Here the magnetic field lines are traced from

a geodetic height h above a given point of the Earth. QD coordinates models the Earth as a geoid as in the original definition, but defines the latitude in terms of the mean radius of the Earth R_E instead of the equatorial radius R_{eq}. Equation (4.9) is mapping along dipole field to R_{eq} while equation (4.12) is a mapping along a dipole field to $R_E + h$. The mapping of QD latitude is not field-aligned, but almost. The QD latitude is given by

$$\lambda_{qd} = \pm \arccos \sqrt{\frac{R_E + h}{R_E + h_a}} \tag{4.12}$$

The Earth magnetic field deviates from a dipole field and this implies that the coordinate system is non-orthogonal. A point in a non-orthogonal coordinate system can be defined in terms of so-called base vectors and Richmond [57] showed mathematically how electrodynamics can be described correctly in a a non-orthogonal coordinate system using base vectors. The magnetic perturbations from ionospheric current measured on the ground are expressed as

$$N_{qd} = \frac{\mathbf{f_1} \cdot \Delta \mathbf{B}}{F} \tag{4.13}$$

$$E_{qd} = \frac{\mathbf{f_2} \cdot \Delta \mathbf{B}}{F} \tag{4.14}$$

where N_{qd} and E_{qd} are the magnetic perturbations in the northward and eastward direction respectively. In equations (4.13) and (4.14) the vectors $\mathbf{f_1}, \mathbf{f_2}$ and F given by equations (6.6), (6.7) and (6.9) in Richmond [57].

$$\mathbf{f_1} = -(R_E + h)\mathbf{k} \times \nabla \lambda_{qd} \tag{4.15}$$

$$\mathbf{f_2} = (R_E + h) \cos \lambda_q \mathbf{k} \times \nabla \varphi_{qd} \tag{4.16}$$

$$F = \mathbf{f_1} \times \mathbf{f_2} \cdot \mathbf{k} \tag{4.17}$$

The vector $\mathbf{k}$ is an unit vector pointing upwards, F is a scaling factor, $\nabla \lambda_a$ is the gradient of the latitude and $\nabla \varphi_a$ is the gradient of the longitude. The $\mathbf{f_1}$ and $\mathbf{f_2}$ vectors are horizontal vectors tangent to contours of constant λ_{qd} and φ_{qd}, respectively.

M(110) Coordinates at 110 km for 1995.0
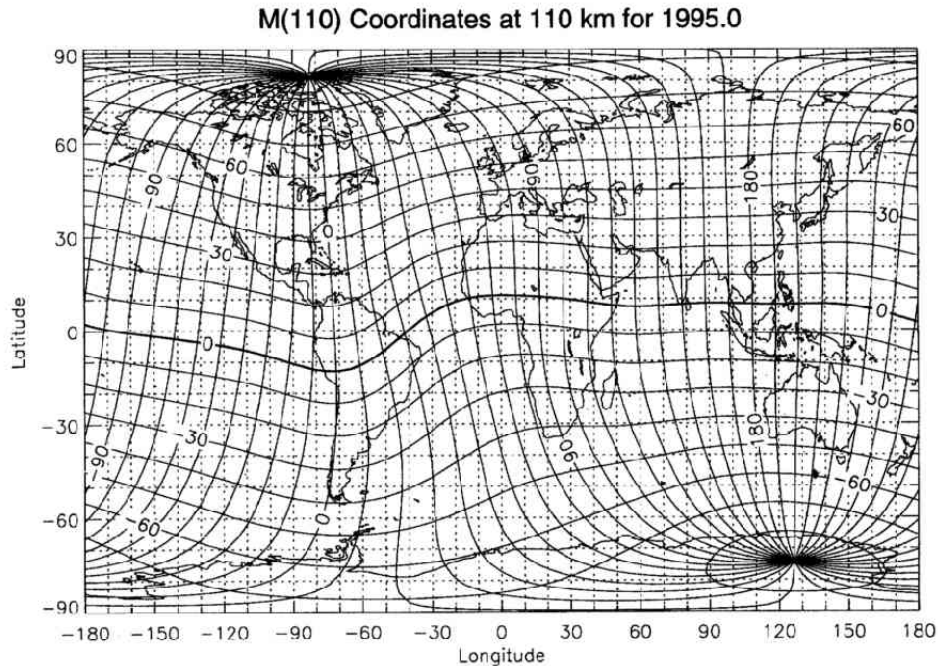
FIGURE 4.3: Figure of the apex coordinates at altitude 110 km in epoch 1995 [57].

4.0.3.1 Interpretation of N_{qd}

Our analysis will be focused on N_{qd} component because of its geometric interpretation. Equation (4.13) can be rewritten as

$$N_{qd} = \frac{\hat{f}_2 \cdot \mathbf{B}_{geo}}{\cos\psi} \frac{1}{|f_1|} \tag{4.18}$$

where ψ is the angle between $\mathbf{f}_2$ and $\mathbf{k} \times \mathbf{f}_1$ and $\hat{f}_2$ is a unit vector in the $\mathbf{f}_2$ direction. Gasda and Richmond [26] defined the factor $1/|f_1|$ as the *width factor* and can be understood as a scaling factor. Laundal et al. [43] interpret $1/|f_1|$ as a measure of QD length per geographic length along $\mathbf{k} \times \mathbf{f}_1$. This factor can be thought of as a scaling factor which compensate for variations in latitudinal extent where zonal ionospheric currents flow. If uniform current flow in the eastward direction in QD-coordinates then the current density will be constant in a QD-grid but the current density will vary with the spacing of contours of constant λ_{qd} in a geographic grid.

4.0.4 Coordinate transformation

Since $\mathbf{f}_1$ and $\mathbf{f}_2$ are given in geographic coordinates by Emmert et al. [18], the magnetic perturbation vectors (4.13) and (4.14) requires $\Delta\mathbf{B}$ given in geographic coordinates as input but our magnetic perturbation data are given in the NEZ-coordinate system. This implies that the transformation is a two step procedure; first convert NEZ-coordinates into geographic coordinates and then geographic coordinates into QD-coordinates.

The first step in the transformation is rotating the magnetic perturbations form SuperMAG-coordinates $\Delta\mathbf{B}_{sm}$ into geographic coordinates $\Delta\mathbf{B}_{geo}$ using a rotation matrix R.

$$\Delta\mathbf{B}_{geo} = R\Delta\mathbf{B}_{sm} \tag{4.19}$$

where the rotation matrix R is given by

$$R = \begin{pmatrix} \cos\alpha & -\sin\alpha & 0 \\ \sin\alpha & \cos\alpha & 0 \\ 0 & 0 & 1 \end{pmatrix} \tag{4.20}$$

where α is the IGRF declination angle at a given magnetometer station. See Figure 4.4 for illustration.
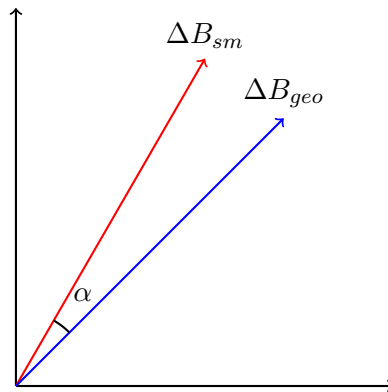
FIGURE 4.4: Rotation from SuperMAG-coordinates to geographic coordinates

When the perturbation has been rotated into geographic coordinates, apex conversion can be initiated. We have made two assumptions 1) the SuperMAG N component is along the IGRF field model and 2) the geodetic height h of the magnetometers is zero.

4.0.5 Magnetic Local Time

It is often more convenient to organize data with respect to the position of the Sun due to the solar wind - magnetosphere coupling. *Magnetic Local Time*(MLT) is divided into 24 hours where one hour MLT corresponds to 15° magnetic longitude.
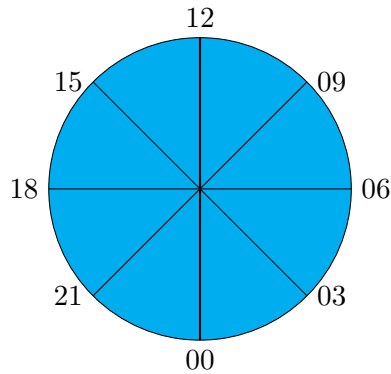
FIGURE 4.5: Numerical values indicates MLT given in hours. The Sun is toward MLT=12 (noon) and magnetic midnight is at MLT=00. MLT dawn and dusk is at MLT=6 and MLT=18 respectively

We have used following definition of MLT

$$\text{MLT} = (\varphi_{qd} - \varphi_{cd,\hat{s}})/15 + 12 \tag{4.21}$$

where φ_{qd} is QD longitude and $\varphi_{cd,\hat{s}}$ is longitude of the subsolar point given in Centerd Dipole coordinates (Russell [61]). This definition, from Laundal and Richmond [42] implies that MTL describes the alignment of the dipole part of the Earth with the Sun.

4.1 Conjugate SuperMAG stations

We define conjugate points as point lying on the same magnetic longitude and opposite signs of magnetic latitude given in QD coordinates. High latitude electrodynamic is governed more by magnetic latitude than longitude hence we have accept an error margin of 1° latitude and 1 MLT longitude. With these criteria we searched for SuperMAG stations poleward of 60° absolute latitude and we identified 19 stations in SH and 18 stations in NH. In total we found 27 conjugate pairs. There was not a one-to-one correspondence between the pairs. For example, the station in NH with International Association of Geomagnetism and Aeronomy (IAGA) code GHB is paired to the stations B15, B16, B17 and B18. When excluding duplicates we are left with 13 unique conjugate pairs.

4.1.1 Location of Stations

The majority of the stations in SH are located in Antarctica. In NH the stations can be found along the coast of Greenland, Jan Mayen, Svalbard, Canada and Alaska. A map showing the location of each SuperMAG magnetometer station can be found in Figure 4.6a. The magnetic latitudes in NH and SH are given in Figure 4.6b and 4.6c respectively.
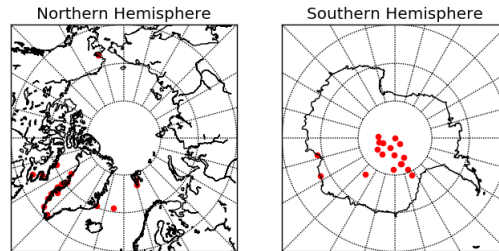
(A) Each red dot indicates a position of a SuperMAG magnetometer station.
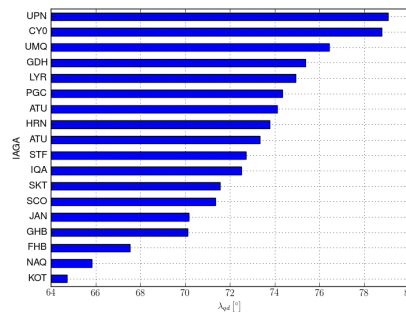
(B) Magnetic latitudes of SuperMAG stations in NH

(C) Magnetic latidues of SuperMAG stations in SH

The error margin we introduced implies that the conjugate station pairs are longitudinally displace with up to ± 1 MLT which is equivalent of several hundreds of kilometres. This displacement means that we do not measure the current exactly at magnetic conjugate

points. How this displacement affects the correspondence is not known and is one of our research topics. A plot of the longitudinal displacement is showed in Figure 4.6.
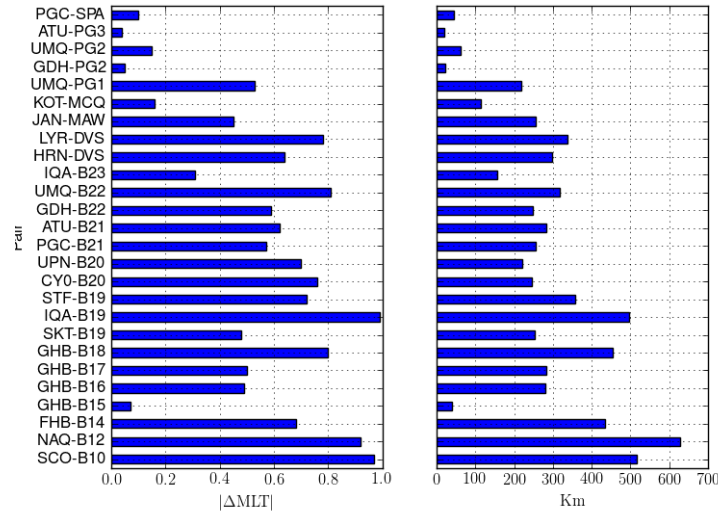
FIGURE 4.6: The plot on the left shows longitudinal displacement of each magnetometer station pair given MLT and the plot on the right shows the equivalent displacement given in km.

4.1.2 Data from Stations

The SuperMAG collaboration has collected magnetometer data from 1980 but SH is poorly covered. The earliest magnetometer observations in our dataset comes from the station pair JAN-MAW covered from 1991 to 2005. Many stations in SH became operational quite recent. For example, the stations PG1, PG2 and PG3 have only data from the year 2013. Of course this causes data loss when requiring simultaneous measurements from the station pairs. Our largest dataset is the conjugate pair JAN-MAW which has simultaneous measurements spanning from 1991-01-01 to 2000-12-30 with 6914036 1 minute resolution data-points. On the other hand, our smallest dataset is ATU-PG3 which has merely simultaneous measurements from 2013-01-05 to 2013-01-08 with 4321 1 minute resolution data-points. Additionally, we selected data with relevant parameters from our datasets. These parameters were solar zenith angles χ when both conjugate points experienced darkness, IMF B_z southward and in many cases low IMF B_y. These requirements imposed great reductions in our datasets, which is showed in Figure 4.7 with JAN-MAW as an example.

What remains in JAN-MAW after all these parameter restrictions is 144236 1 minute resolution data-points, which is only 2 % of the original data-set. Large datasets such as JAN-MAW might have enough data left in order to be statistical significant, but smaller
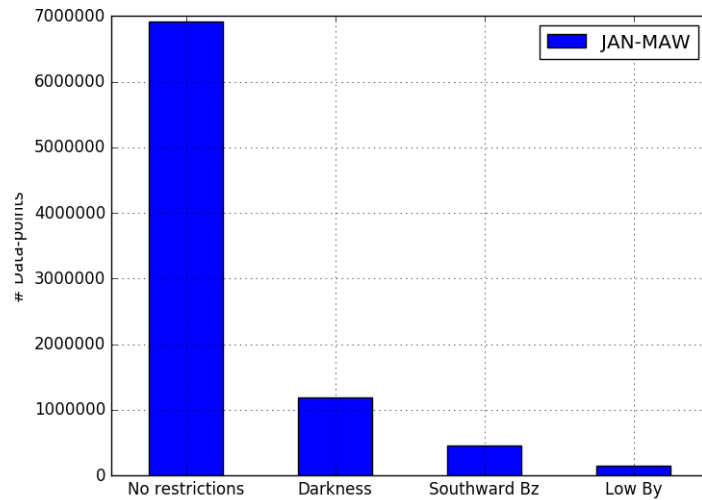
FIGURE 4.7: Selecting data with relevant parameters reduces the number of data-points substantially. The leftmost columns shows the number of data-points with no parameter restrictions. When we select solar zenith angles greater than 90° for both stations then the dataset is reduced ("Darkness" column). Further restriction is made when IMF B_z is restricted to be southward orientated ("Southward Bz" column). In many cases we are also restricted to low IMF B_y. In the column "Low By" we have selected data when the absolute value of IMF B_y is less than 2 nT.

datasets may not. ATU-PG3, for example, did not have any data when both stations experienced darkness simultaneously. Figure 4.8 shows how much data the magnetometer pair have before and after parameter restriction.
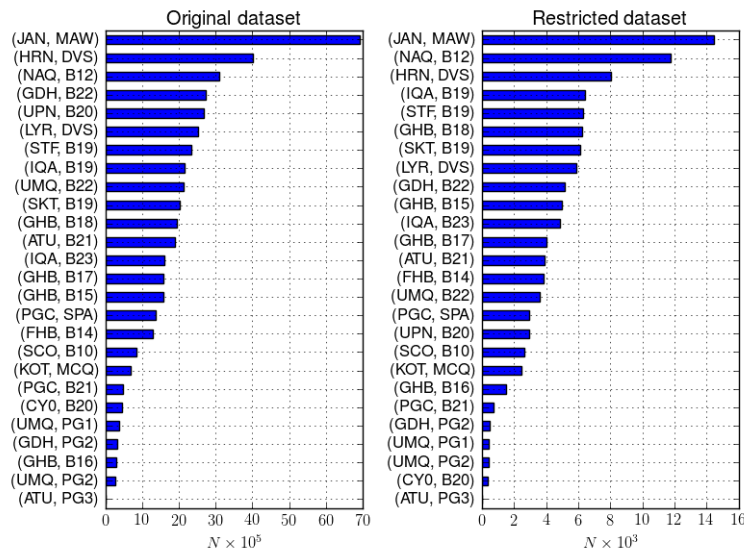
FIGURE 4.8: The figure on the left shows number of datapoints with not parameter restrictions. The figure on the right shows the remaining datasets after the parameter restrictions mentioned above

The requirement that both stations lie in dark regions implies that the majority of our

dataset is covered during equinox. During summer of winter is it very likely that one station in NH is sunlit while the conjugate station in SH is in darkness. For example, 60% of the data of HRN-DVS was measured during the equinox months.

4.2   Linear relationship between magnetic perturbations

Figure 4.9 shows the density at log scale of data points from JAN and MAW, in hexagonal bins defined in terms of the magnetic field measurements. The x-axis shows the value of N_{qd} measured by MAW and the y-axis shows values of N_{qd} measured by JAN. The colorbar indicate the number of data point in a given cell in a logarithmic scale.
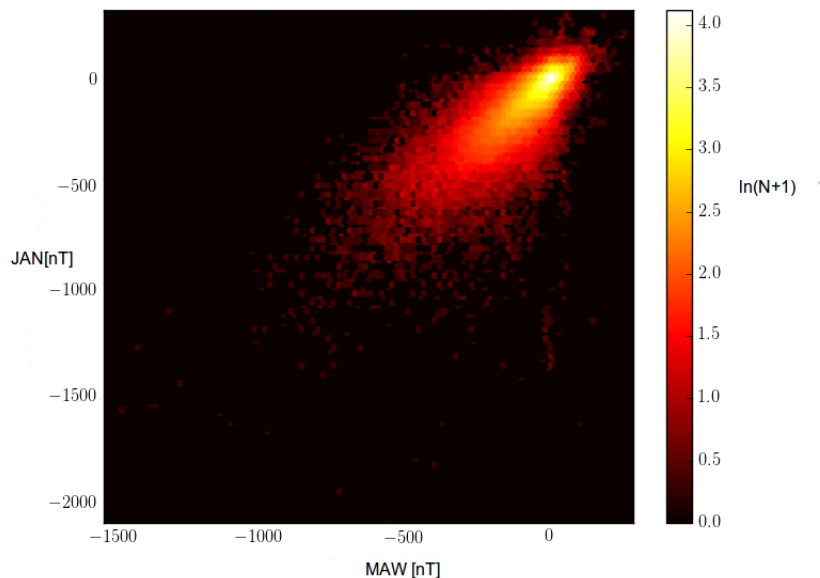
FIGURE 4.9: Hexbinplot of the station pair JAN-MAW. The figure is made by a grid of hexagonal cells containing N number of data in each cell. The x-axis shows the magnetic perturbation measured by MAW and the y-axis shows magnetic perturbations measured by JAN. The colourbar indicates the amount of data in each hexbin cell.

By visual inspection of plots of the data set, similar to 4.9, we argue that the magnetic perturbation have a linear relationship, and statistical methods, such as linear regression and correlation, is applicable. However, we acknowledge some weaknesses with this assumption: a large amount of data clustered close to $0nT$. This is due to the design of SuperMAG processing technique which removes the baseline. There is also a large variation in the data set, especially at large perturbations.

Notice that strong magnetic perturbations have negative values. This is caused by westward electrojets flowing above the magnetometer stations where current flowing strictly westward would produce magnetic perturbation in the southward direction i.e. -N_{qd}.

Chapter 5

Results and Discussion

Our results are presented and discussed in this chapter. First, we theoretically and empirically determine a limit solar zenith angle that defines darkness. In the theoretical approach we modelled the ionosphere as an thin layer at a height above the surface of the Earth and calculated how many degrees below the horizon is required to be in darkness. In the empirical method we identified the limit of which solar zenith angle were magnetic perturbations were well correlated. The theoretical required a more strict limit of solar zenith angle and we found no advantages in using this definition. Therefore, we used the limits we found empirically.

We also examined how the IMF B_y affects the correlation of magnetic perturbations. The IMF B_y is associated with forces able to shift the foot points of closed magnetic field lines. At first, we expected this effect to improve correlation because this makes the stations more conjugated, but we found the opposite. We suspect that this has to do with asymmetric current systems associated with IMF B_y.

The ionospheric conductance is scaled with the strength of the magnetic field. Our results is consistent with this and we offer a method of determining the scaling factor. There is however statistical uncertainties related to our dataset which make this determination rather difficult.

5.1 Sunlight Terminator

Sunlight have effects on ionospheric currents by affecting ion production (Chapman [10], Chapman and Mian [11])and ionospheric conductance (Moen and Brekke [49], Richmond [57], Robinson and Vondrak [58]. For a given moment two magnetic conjugate points generally experience different solar zenith angles and different currents for this reason. Also, the difference in pole offsets cause difference in exposure to sunlight. The polar region in SH has an magnetic apex pole more than 8.5° away from the geographic pole compared to the polar region in NH. This is illustrated in Figure 5.1
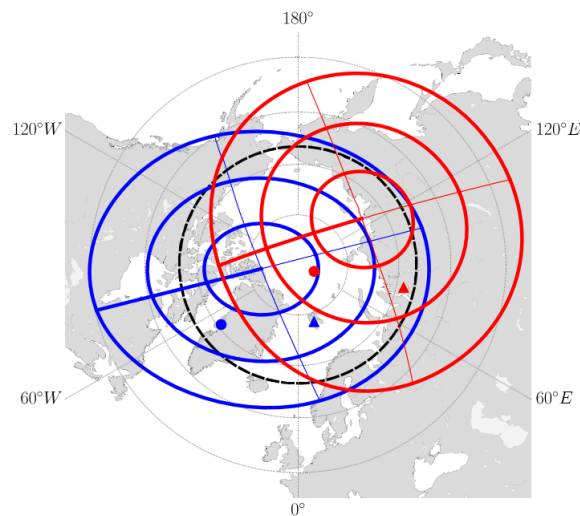
FIGURE 5.1: QD circles of latitude $\pm 60°, \pm 70°, \pm 80°$ from both hemispheres projected on NH. Red corresponds to SH and blue corresponds to NH. Markers indicates conjugate points. Figure adapted from Laundal and Richmond [42]

Difference in pole offset means that as the Earth rotates the polar region in SH experience larger daily variations of sunlight than in NH. The upper figure in Figure 5.2 shows how the hemispheric fraction of sunlight varies with UT. The lower figure shows the daily minimum and maximum sunlit fraction at equinox.

Due to the differences in sunlight conditions we chose to perform our analysis when both station are in darkness. The determination of darkness was approached using two methods: a simple theoretical model in section 5.1.0.1 and measurements from magnetic perturbation data in section 5.1.0.2.
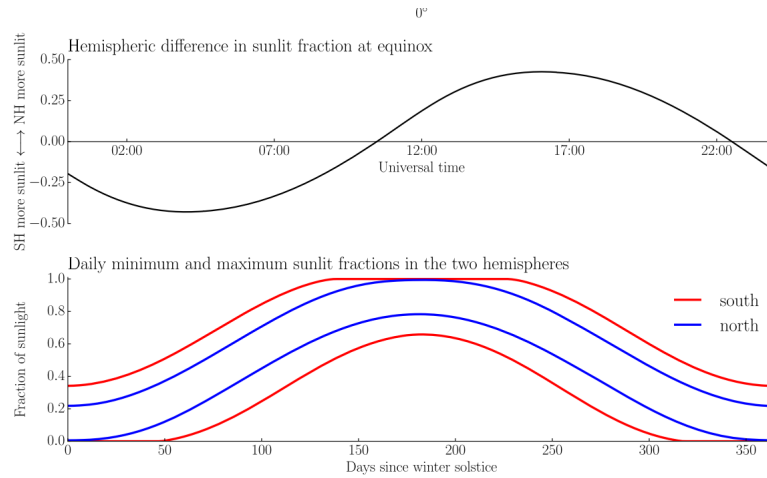
FIGURE 5.2: The upper plot shows the UT variation of hemispheric fraction of sunlight at $\pm 60°$ at equinox. The lower plot shows the variation of sunlight exposure over the year. The curves shows daily minimum and maximum fraction of the region poleward of $60°$ which is sunlit. Figure by Laundal and Richmond [42]

5.1.0.1   Theoretical

In Figure 5.3 we have used a simple model of the ionosphere as an infinite thin layer at a height h above the surface of the Earth. We used this model to determine the solar zenith angle where the ionosphere is in darkness. At an altitude of $h = 100$km we find that the ionosphere is in darkness at at $10°$ below the horizon i.e. $\chi = 100°$. The effects of sunlight scattering are ignored, however, this is the same definition of darkness as used by Friis-Christensen et al. [22].
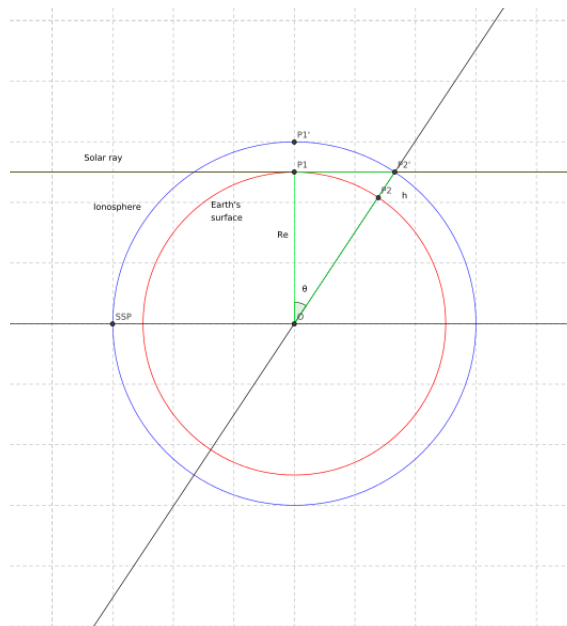
FIGURE 5.3: The ionosphere is modelled as an infinite thin shell at a height h above the surface of the Earth. The angle θ defines when $P2'$ is in darkness

5.1.0.2 Empirical

Due to the differences in sunlight in the hemispheres we examined how the magnetic perturbations at magnetic conjugate points correlates during different sunlight conditions. We used the following procedure: For a given magnetometer station, the solar zenith angles χ ranging from $40°$ to $140°$ were divided into bins of $5°$ sized intervals. The measurements on N_{qd} were then grouped into their corresponding solar zenith angle bins. The same procedure was performed for the conjugate magnetometer station. Calculations of N_{qd} correlation coefficients for each solar zenith bin with the conjugate station bins were performed. We required at least 1000 data points in a bin in order to calculate the correlation coefficient in order to keep statistical significance. This gives a 2 dimensional matrix of N_{qd} correlation coefficients which can be visualised as a contour plot.

We used the Pearson correlation coefficient r_{xy} in our calculations. The Person correlation coefficient for dataset $\mathbf{x}$ and $\mathbf{y}$ is defined by

$$r_{xy} = \frac{\sum_{i=1}^{n}(x_i - \bar{x})(y_i - \bar{y})}{\sqrt{\sum_{i=1}^{n}(x_i - \bar{x})^2) \sum_{i=1}^{n}(y_i - \bar{y})^2)}} \tag{5.1}$$

where n is the number of elements in each data set, x_i is the i-th element in $\mathbf{x}$ and $\bar{x}$ is the arithmetic mean of $\mathbf{x}$. Similar notation is used for data set $\mathbf{y}$ It is important to note that Person correlation is sensitive to outliers and a more robust correlation method could be used instead. We leave this for future research.

The procedure above was performed for each conjugate stations pair. Below we have showed the results starting with station pair at lowest magnetic latitude (KOT-MCQ at $\lambda_{qd} = 64°$) then moving poleward to the station pair with highest magnetic latitude (UPN-B20 at $\lambda_{qd} = 79°$). ATU-PG3 was left out because the dataset for this station pair was empty with our restrictions mention above. We found that the correlation contours shows different features depending on location.

Magnetic perturbations measured in latitude $\lambda_{qd} \in (64°, 71°)$ are almost always highly correlated regardless of solar zenith angles. The correlations are only poorly correlated when χ_{NH} and χ_{SH} deviate much from each other. This suggest that magnetic perturbation correlations are determined by currents not related to photoionization. These stations lie statistically in the auroral zone and the auroral electrojets flows in this region.

Stations poleward only shows high correlation when both stations are in darkness and above a certain angle. For example, SCO-B10 in Figure 5.12 seems to be well correlated for solar zenith angles above $80°$. Stations located at higher latitudes seems to require even higher solar zenith angles to archive high correlation. HRN-DVS is well correlated

above 85° and UMQ-B22 correlates well close to 90°. One interpretation of the high correlation below 90° is that these regions are dark enough to neglect photo ionization. Ion production by solar illumination is in fact dominant below 80° (Moen and Brekke [49], Richmond [57]). Figures of the station pairs are given below.

5.1.0.3 Auroral Zone

The following SuperMAG stations are located in magnetic latitudes $64° < \lambda_{qd} < 71°$. These stations show high correlation nearly independent of solar zenith angle. We have however defined these stations to be in darkness at solar zenith angles above 80° where sunlight ceases to be the dominant source of ion production.
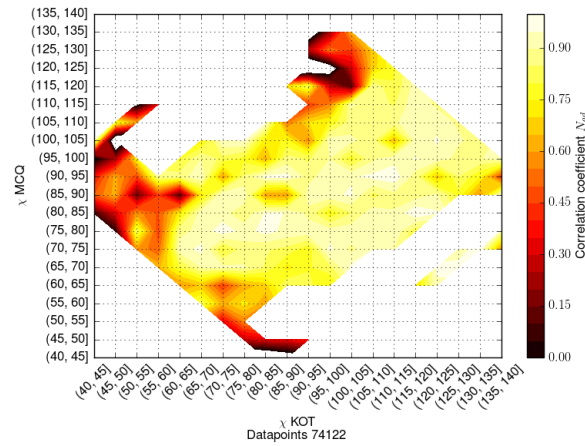
FIGURE 5.4: Correlation contours of KOT-MCQ
KOT $(\lambda_{qd}, \varphi_{qd}) = (64.73°, -108.41°)$
MCQ $(\lambda_{qd}, \varphi_{qd}) = (-64.15°, -111.89°)$
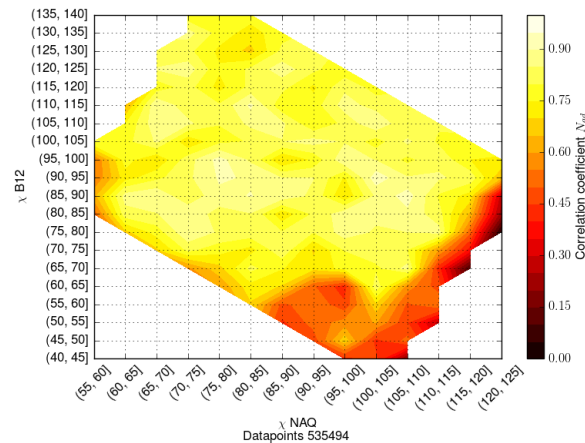
FIGURE 5.5: Correlation contours of NAQ-B12
NAQ $(\lambda_{qd}, \varphi_{qd}) = (65.82°, 43.16°)$
B12 $(\lambda_{qd}, \varphi_{qd}) = (-64.62°, 29.03°)$
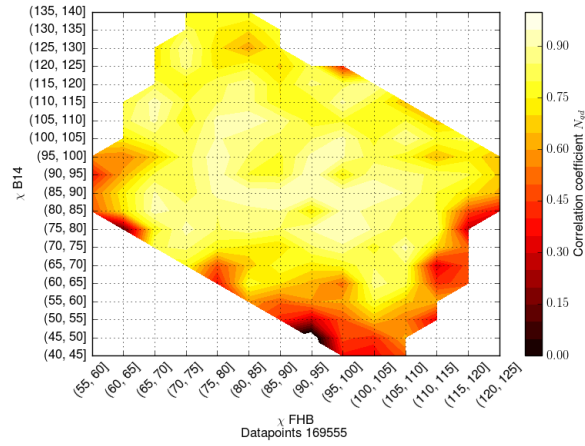
FIGURE 5.6: Correlation contours of FHB-B14
FHB $(\lambda_{qd}, \varphi_{qd}) = (67.53°, 38.98°)$
B14 $(\lambda_{qd}, \varphi_{qd}) = (-66.24°, 28.68°)$
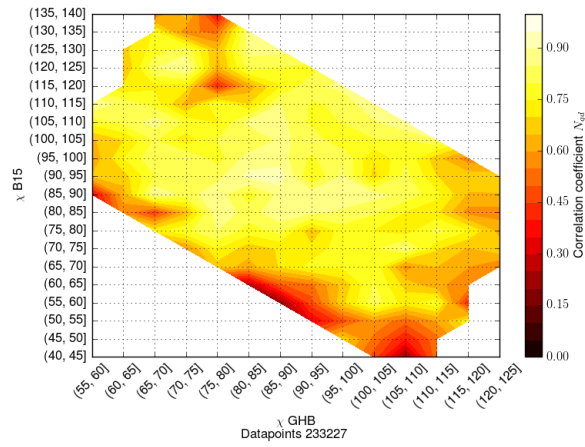
FIGURE 5.7: Correlation contours of GHB-B15
GHB $(\lambda_{qd}, \varphi_{qd}) = (70.12°, 37.82°)$
B15 $(\lambda_{qd}, \varphi_{qd}) = (-68.55°, 36.51°)$
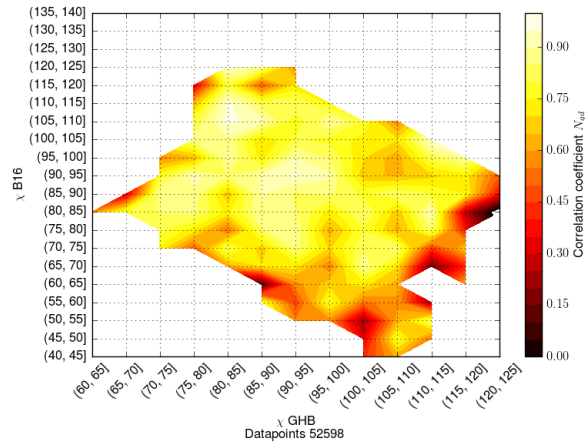
FIGURE 5.8: Correlation contours of GHB-B16
GHB $(\lambda_{qd}, \varphi_{qd}) = (70.12°, 37.82°)$
B16 $(\lambda_{qd}, \varphi_{qd}) = (-68.38°, 30.13°)$
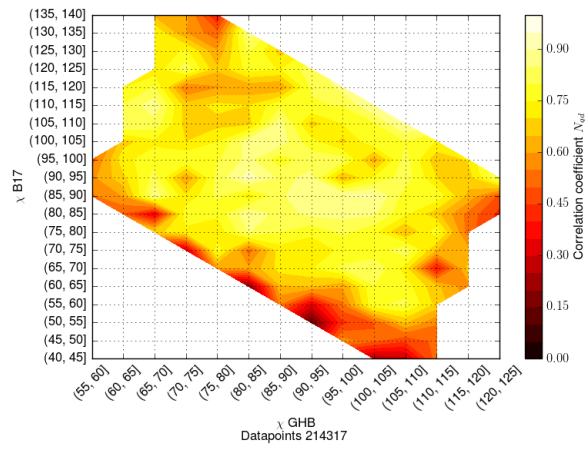
FIGURE 5.9: Correlation contours of GHB-B17
GHB $(\lambda_{qd}, \varphi_{qd}) = (70.12°, 37.82°)$
B17 $(\lambda_{qd}, \varphi_{qd}) = (-68.46°, 30.11°)$
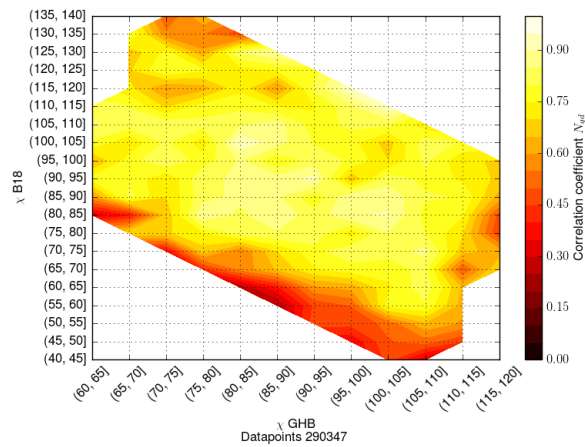
FIGURE 5.10: Correlation contours of GHB-B15
GHB $(\lambda_{qd}, \varphi_{qd}) = (70.12°, 37.82°)$
B18 $(\lambda_{qd}, \varphi_{qd}) = (-69.07°, 25.55°)$
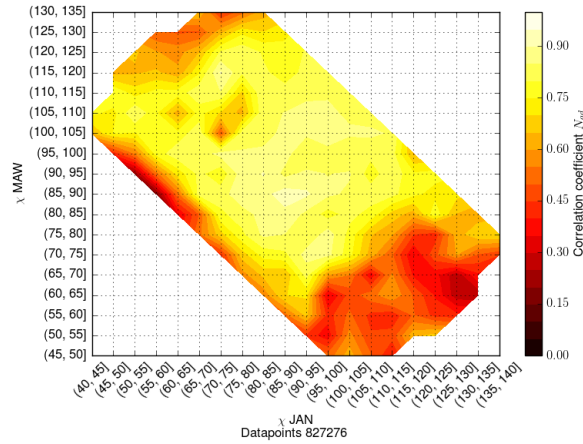
FIGURE 5.11: Correlation contours of JAN-MAW
JAN $(\lambda_{qd}, \varphi_{qd}) = (70.17°, 84.55°)$
MAW $(\lambda_{qd}, \varphi_{qd}) = (-70.01°, 90.16°)$

5.1.0.4 Polar cap stations

The following SuperMAG stations are located in the polar cap. These correlations of these stations seem to be more determined by the sunlight conditions than stations in the auroral zone. We found that the correlations in most of the polar cap stations were better correlated when both conjugate magnetometer station were in darkness and worse when the stations happened to be in sunlit-sunlit or sunlit-dark conditions. During daytime the conjugate magnetometer stations are exposed to different sunlight conditions and the ionospheric currents will therefore be different. This is eliminated when stations move to dark regions and correlation improves.
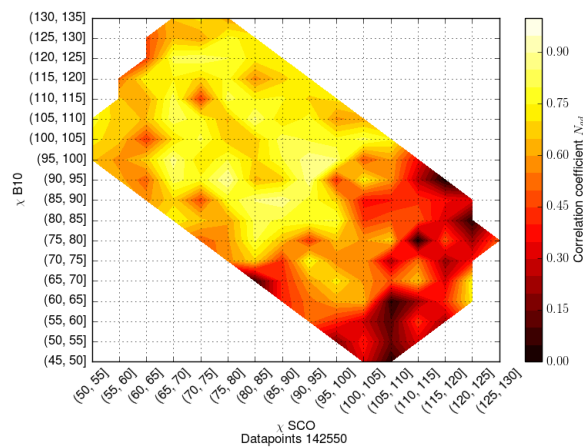
FIGURE 5.12: Correlation contours of SCO-B10
SCO $(\lambda_{qd}, \varphi_{qd}) = (71.35°, 71.95°)$
B10 $(\lambda_{qd}, \varphi_{qd}) = (-68.55°, 36.51°)$
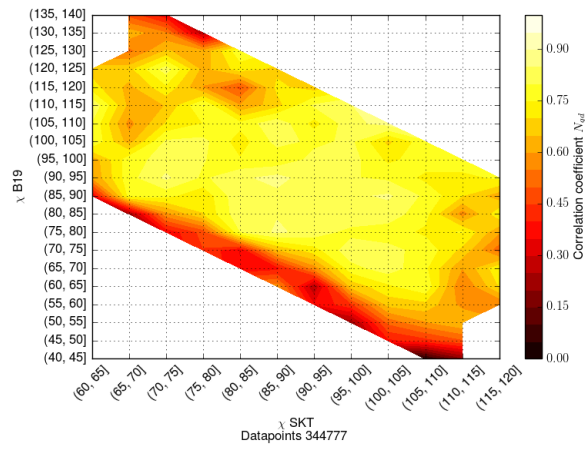
FIGURE 5.13: Correlation contours of SKT-B19
SKT $(\lambda_{qd}, \varphi_{qd}) = (71.57°, 37.22°)$
B19 $(\lambda_{qd}, \varphi_{qd}) = (-71.08°, 29.67°)$
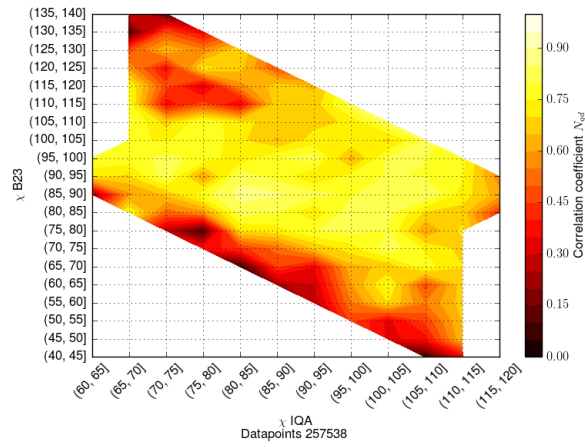
FIGURE 5.14: Correlation contours of IQA-B23
IQA $(\lambda_{qd}, \varphi_{qd}) = (72.52°, 14.82°)$
B23 $(\lambda_{qd}, \varphi_{qd}) = (-72.08°, 29.67°)$
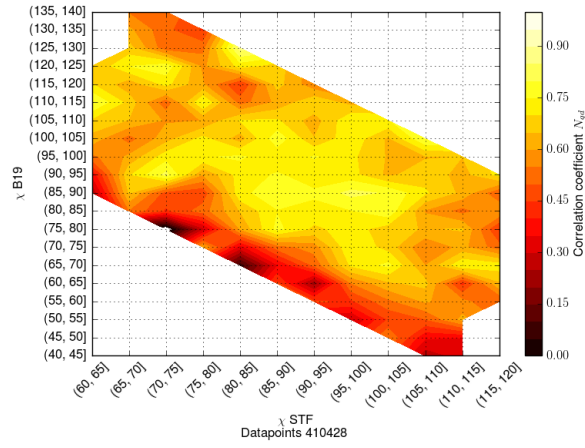
FIGURE 5.15: Correlation contours of STF-B19
STF $(\lambda_{qd}, \varphi_{qd}) = (72.73°, 41.00°)$
B19 $(\lambda_{qd}, \varphi_{qd}) = (-71.08°, 29.67°)$
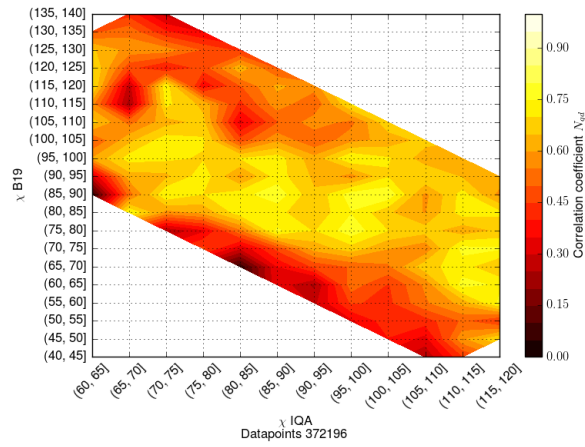
FIGURE 5.16: Correlation contours of IQA-B19
IQA $(\lambda_{qd}, \varphi_{qd}) = (72.52°, 14.82°)$
B19 $(\lambda_{qd}, \varphi_{qd}) = (-71.08°, 29.67°)$
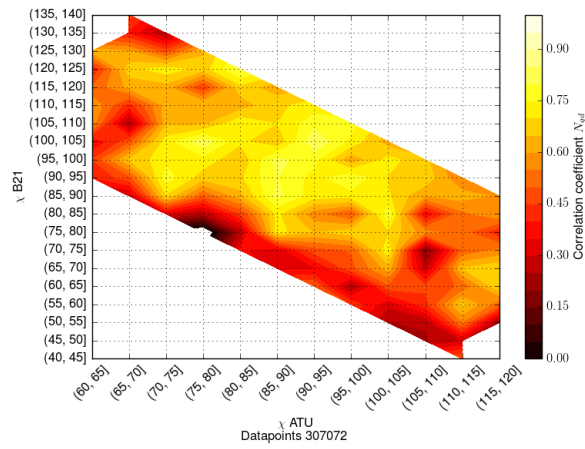
FIGURE 5.17: Correlation contours of ATU-B21
ATU $(\lambda_{qd}, \varphi_{qd}) = (74.12°, 38.31°)$
B21 $(\lambda_{qd}, \varphi_{qd}) = (-73.28°, 28.60°)$
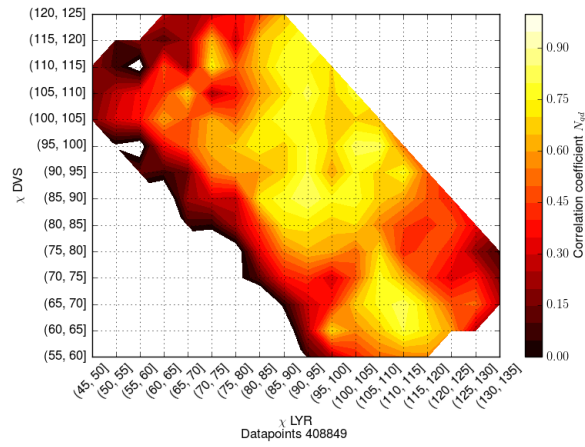
FIGURE 5.18: Correlation contours of LYR-DVS
LYR $(\lambda_{qd}, \varphi_{qd}) = (74.36°, 20.05°)$
DVS $(\lambda_{qd}, \varphi_{qd}) = (-73.28°, 28.60°)$
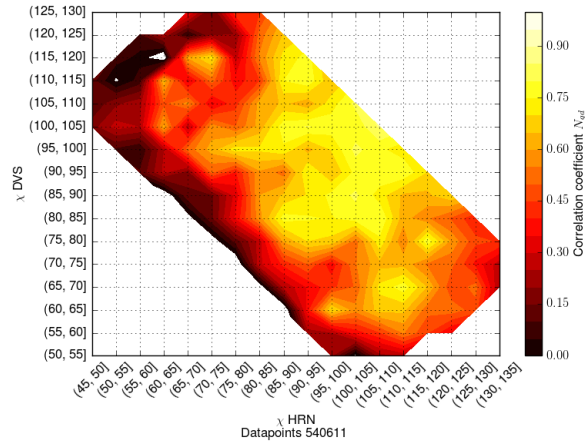
FIGURE 5.19: Correlation contours of HRN-DVS
HRN $(\lambda_{qd}, \varphi_{qd}) = (73.78°, 110.45°)$
DVS $(\lambda_{qd}, \varphi_{qd}) = (-74.37°, 100.20°)$
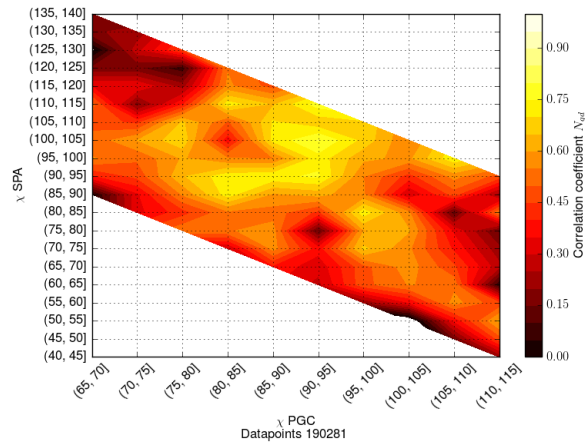
FIGURE 5.20: Correlation contours of PGC-SPA
PGC $(\lambda_{qd}, \varphi_{qd}) = (74.36°, 20.05°)$
SPA $(\lambda_{qd}, \varphi_{qd}) = (-73.87°, 18.58°)$
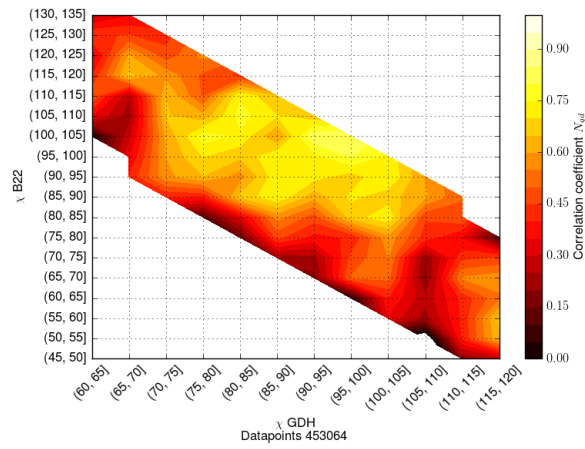
FIGURE 5.21: Correlation contours of GDH-B22
GHD $(\lambda_{qd}, \varphi_{qd}) = (75.37°, 39.62°)$
B22 $(\lambda_{qd}, \varphi_{qd}) = (-75.43°, 30.34°)$

The follow stations have little data when both are in darkness. This is either due to few measurements or the stations are located at positions such that one station is in sunlit regions while the other is in dark regions for long time periods.
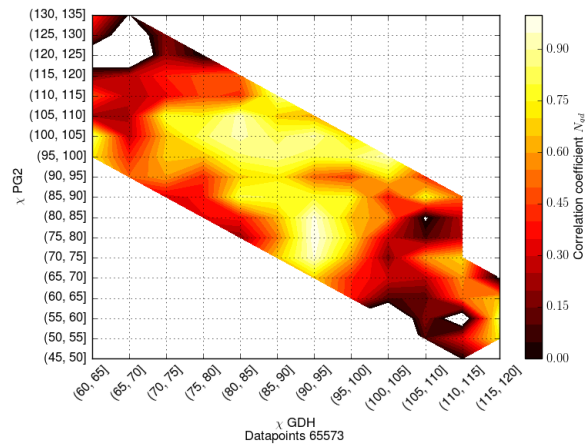
FIGURE 5.22: Correlation contours of GDH-PG2
GHD $(\lambda_{qd}, \varphi_{qd}) = (75.37°, 39.62°)$
PG2 $(\lambda_{qd}, \varphi_{qd}) = (-75.31°, 39.11°)$
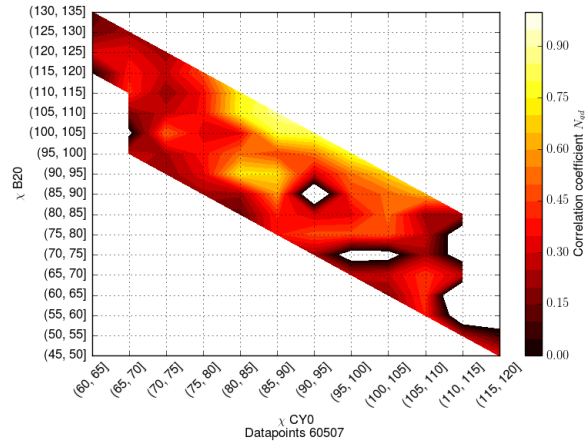
FIGURE 5.23: Correlation contours of CY0-B20
CY0 $(\lambda_{qd}, \varphi_{qd}) = (78.78°, 18.51°)$
B20 $(\lambda_{qd}, \varphi_{qd}) = (-77.62°, 29.78°)$
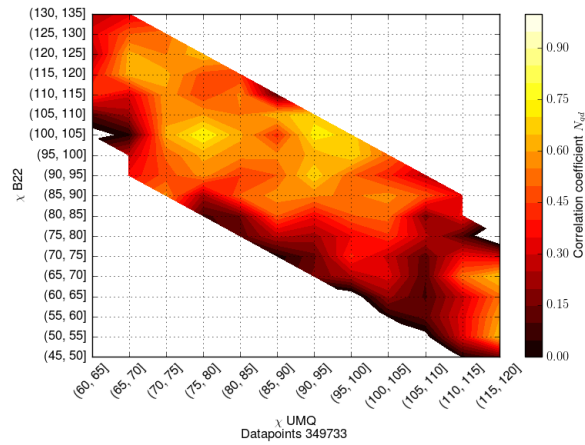
FIGURE 5.24: Correlation contours of UMQ-B22
UMQ $(\lambda_{qd}, \varphi_{qd}) = (76.44°, 42.89°)$
B22 $(\lambda_{qd}, \varphi_{qd}) = (-75.43°, 30.34°)$
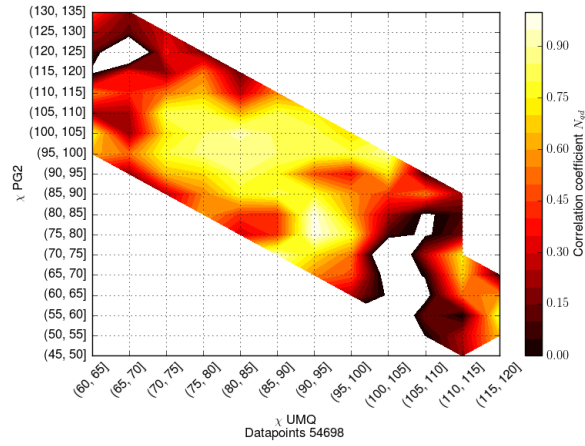
FIGURE 5.25: Correlation contours of UMQ-PG2
UMQ $(\lambda_{qd}, \varphi_{qd}) = (76.44°, 42.89°)$
PG2 $(\lambda_{qd}, \varphi_{qd}) = (-75.31°, 39.11°)$
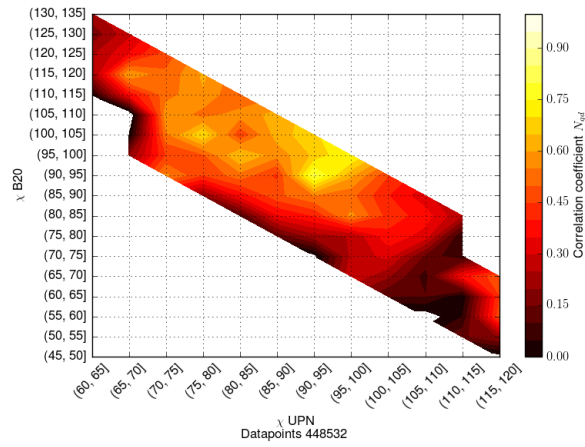
FIGURE 5.26: Correlation contours of UPN-B20
UPN $(\lambda_{qd}, \varphi_{qd}) = (79.07°, 40.83°)$
B20 $(\lambda_{qd}, \varphi_{qd}) = (-77.62°, 29.78°)$
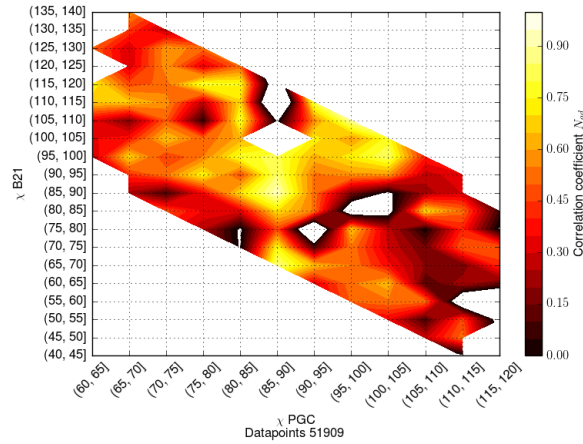
FIGURE 5.27: Correlation contours of PGC-B21
PGC $(\lambda_{qd}, \varphi_{qd}) = (74.36°, 20.05°)$
B21 $(\lambda_{qd}, \varphi_{qd}) = (-73.28°, 28.60°)$
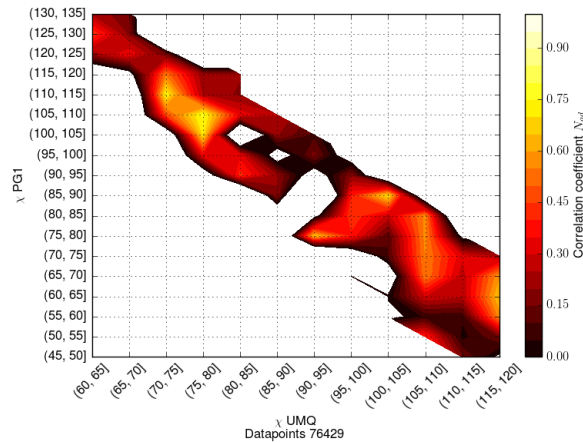
FIGURE 5.28: Correlation contours of UMQ-PG1
UMQ $(\lambda_{qd}, \varphi_{qd}) = (76.44°, 42.89°)$
PG1 $(\lambda_{qd}, \varphi_{qd}) = (-76.63°, 33.50°)$

By visual inspection of figures 5.4-5.28, we determined the limits for solar zenith angles that defines darkness. In these figures we see that magnetic perturbation are highly correlated ($r \geq 0.7$) for high solar zenith angles. This is indicated as yellow contours, while poorly correlated perturbations ($r < 0.7$) are indicated as red contours. The limit was found as the lowest solar zenith angle at the boundary of yellow and red contours. We acknowledge that this method is only an approximation. UMQ-PG1 is missing because we were not able to determine any limit for this station pair.

Station pair	$\chi[°]$
KOT-MCQ	80
NAQ-B12	80
FHB-B14	80
GHB-B15	80
GHB-B16	80
GHB-B17	80
GHB-B18	80
JAN-MAW	80
SCO-B10	85
SKT-B19	80
IQA-B19	85
IQA-B23	80
STF-B19	85
ATU-B21	85
HRN-DVS	85
PGC-B21	85
PGC-SPA	85
LYR-DVS	85
GDH-B22	85
GDH-PG2	85
UMQ-B22	90
UMQ-PG2	85
CY0-B20	90
UPN-B20	90

TABLE 5.1: Sunlight terminator for each stations pair

The limits we found empirically required lower solar zenith angles than the theoretical $100°$ solar zenith angle limit. The latter limit reduces our data sets and we found no advantages in using this limit. See next section for details. Therefore, we used the limits determined empirically listen in Table 5.1

5.2   IMF B_y effects

A magnetometer station located in NH might be longitudinally displaced from its magnetic conjugate point in the SH. This longitudinal displacement is called *nominal displacement* and is measured in MLT, ΔMLT_{nom}. This displacement should affect the correlation of magnetic perturbations between the hemispheres, because they are making measurements in different regions of the ionospheric equivalent currents systems. Points are magnetic conjugate if they are connected by the same magnetic field line between the hemispheres. Pressure forces associated with IMF B_y are able to shift the position of the magnetic foot points on the night side (Tenfjord et al. [65]). Østgaard et al. [51] reported an empirical equation for the relative longitudinal displacement of the magnetic foot points as function of IMF B_y given by $\Delta\text{MLT}_{imf} = 0.88\sin(B_y/12 \times 90° - 9.3°)$. The total displacement is given by $\Delta\text{MLT}_{tot} = \Delta\text{MLT}_{nom} + \Delta\text{MLT}_{imf}$. Given the right IMF B_y the magnetic foot points can be shifted such that the total displacement is zero. We examine whether the correlation of magnetic perturbation is better at this point.

The equation ΔMLT_{imf} is valid for closed magnetic field lines only. Closed magnetic field lines at high latitudes lie within the auroral zone located at the magnetic latitudes $\sim 60° - 70°$ on the nightside (Feldstein [20]). Therefore, we identified magnetometer stations found at these latitudes and calculated correlation in the process described below.

Measurements of the total displacements ΔMLT were grouped into 10 bins with equally many data points and the mean displacement in each bin was calculated. In each bin the correlation coefficient of N_{qd} component between conjugate stations pair were calculated. We selected station pairs located in the auroral zone, because IMF control of described above is only valid for closed magnetic field lines (Østgaard et al. [50, 51]). The selected IMFB_y values ranging from -12 nT to 16 nT which is the same IMF By domain equation 2.26 were fitted from. We only used data from periods when IMF $B_z < 0$. Values outside this domain would carry statistical uncertainties because we would then extrapolate ΔMLT values. We also only use measurements made in darkness.

This procedure was performed for both low and high magnetic activities in order to account for any possible activity effects. The AL-index is a commonly used parameter to indicate magnetic activity levels. Allen and Kroehl [3] defined disturbed periods as simply $AL \leq -50nT$ but it is important to note that there is no well defined threshold on what AL-index corresponds to high or low magnetic activity (Kamide and Akasofu [33], Rostoker et al. [59]). We have define low magnetic activity as $AL > -50nT$ and high activity as $AL < -500nT$ in order to see a clear difference between the activity

levels. On the left side of figures 5.29a we have shown conditions during low magnetic activity and the right side shows high magnetic activity.

In Figure 5.29a we used $80°$ as the terminator and in Figure 5.29b we used $100°$. This was done in order to spot any effects the choice of solar zenith angle might have the correlations. We did not find any clear indication that correlations are affected significantly by this. Any differences between these figures might be due to the unequal data size shown in Figure 5.29c and 5.29d.
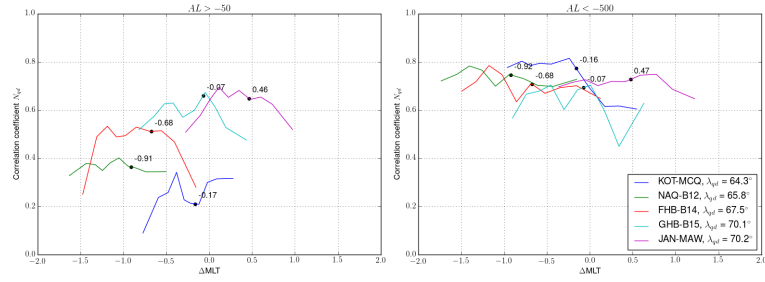
(A) Terminator: $\chi = 80°$
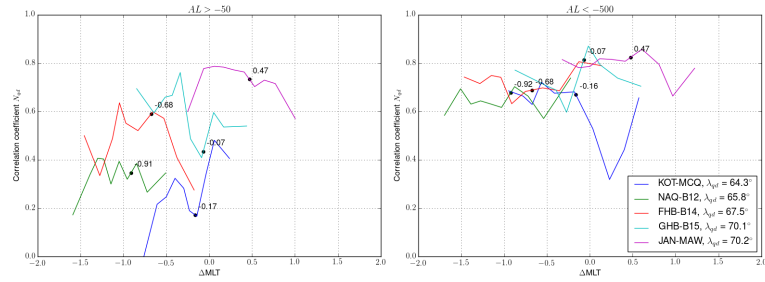
(B) Terminator: $\chi = 100°$
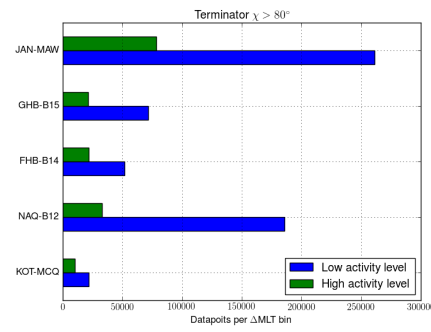
(C) Number of data point in each bin for a given station pair for $\chi > 80°$
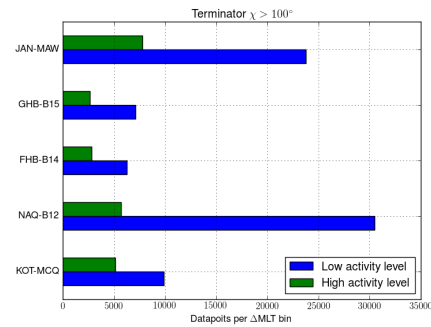
(D) Number of data point in each bin for a given station pair for $\chi = 100°$

FIGURE 5.29: Correlation of ΔMLT for stations in the auroral zone. The sunlit-dark terminator is 80° in Figure 5.29a and 100° in Figure 5.29b. The figures on the left are during weak westward electrojets and the figures on the right are during strong westward currents.

At first we expected optimal correlation when ΔMLT approaches zero, but this was not the case, rather the opposite. In Figure 5.29a we cannot see any clear indication that correlation is highest at ΔMLT $= 0$. Also, the station pair FHB-B14 even had lowest correlations at this point. On the left of Figure 5.29a we can see that the correlation is highest at the nominal conjugate point and decreasing for ΔMLT_{imf}. On the right of Figure 5.29a, which shows high magnetic activity, we see that the correlation is less affected by ΔMLT.

Our interpretation of these results is that during high activity levels, the current systems at these latitudes are the auroral electrojets, which flow longitudinally and are large in spatial extent, and the conjugate magnetometer stations will measure similar magnetic perturbations. During low activity levels the correlations seem to be dependent on effects related to IMF B_y. An interpretation of this is given shortly.

We tested this be grouping magnetic perturbation data by their corresponding IMF B_y values. Then we used a similar correlation procedure as above. If our interpretation is correct, then should the correlation should be highest at IMF $B_y = 0$ and decreasing for larger values of $|$IMF $B_y|$. Our results are shown in Figure (5.30a) and (5.30b).
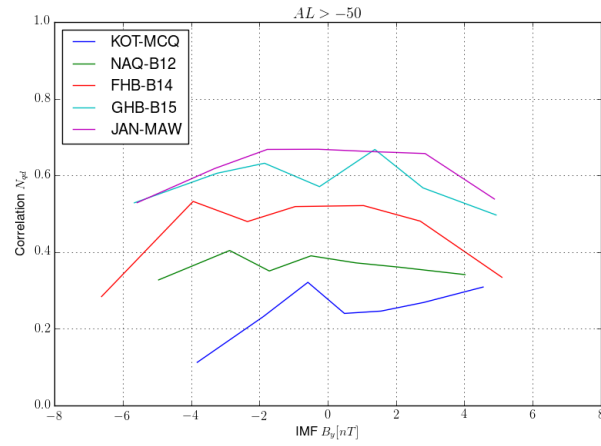
(A) Low activity
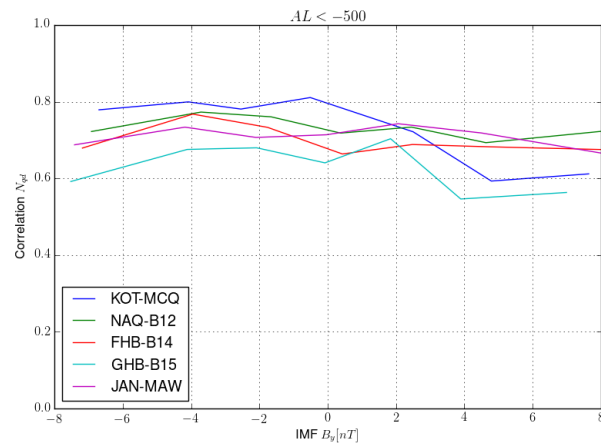
(B) High activity

FIGURE 5.30: Correlation as a function of IMF By

These results are consistent with our interpretation. In Figure (5.30b) we can see that the correlation is high during the entire IMF B_y interval for high activity levels. During low activity, shown in Figure (5.30a), the magnetic perturbations are well correlated on the interval $-2nT <$ IMF $B_y < 2nT$. We suggest using $2nT$ as a threshold for "small" IMF B_y values.

Our explanation for our results is that the correlation is more determined by asymmetric current systems at conjugate points. Cowley [13] showed that the characteristic "banana" and "orange" shaped plasma convection pattern are nearly mirrored at the hemispheres. Since Hall currents flow opposite to the plasma convection, so the Hall currents should then be asymmetric between the hemispheres. Laundal and Richmond [42], Laundal et al. [43] demonstrated that in the dark ionosphere, the currents systems are influenced by Birkeland currents, and Tenfjord et al. [65] found that IMF B_y leads to asymmetric Birkeland currents at conjugate points. These factors indicate that when IMF has a strong B_y component the equivalent currents pattern should be asymmetric between the hemispheres. The magnetic perturbation vectors should then be pointing in different directions with respect to each other and worsening the correlation.
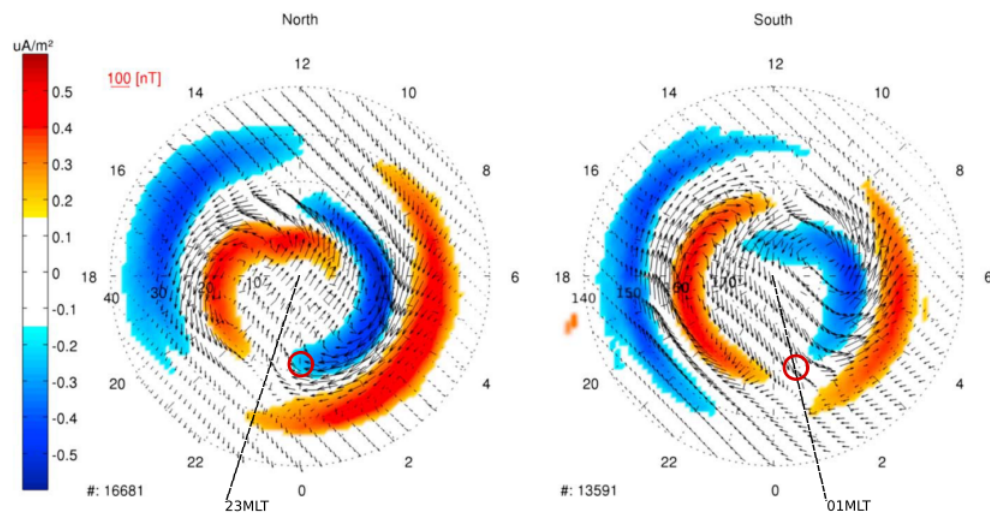
FIGURE 5.31: Birkeland currents and magnetic perturbations are asymmetric at conjugate points when IMF has a strong B_y component. This case shows IMF $B_z < 0nT$ and IMF $B_y > 5nT$. Colours indicate Birkeland current density and vectors indicate measured magnetic perturbations. Figure by Tenfjord et al. [65]

5.3 Effects From Asymmetries in the Magnetic Field

In section 2.6 we discussed that ionospheric current is a function of magnetic field strength B. Richmond [57] and Cnossen et al. [12] found theoretically that ionospheric conductances are scaled with B. To our knowledge, these scaling factors have not been confirmed empirically, and we are not aware of any scaling factors confined to the ionosphere in darkness.

Magnetic perturbation data revealed a linear relationship between δB_{SH} and δB_{NH}. An example of this is given in Figure 4.9. The relation between δB_{SH} and δB_{NH} without the constant term can be expressed on the form

$$\delta B_{SH} = b\,\delta B_{NH} \tag{5.2}$$

where b is the slope of the linear equation which can be obtained by regression analysis. Our datasets contains many outliers and hence motivates a more robust analysis than simple least squares. The slope b in equation (5.2) were therefore found by linear regression with Huber weights. Regression with Huber weights is an iterative scheme designed to reduce sensitivity to outliers (Huber [31]). The weights w_i are defined as

$$w_i = \min\left\{1, \frac{k}{|x_i - \langle x_i \rangle|/\sigma}\right\} \tag{5.3}$$

where k is set equal to 1.5 and $\langle x_i \rangle$ is the mean of the dataset. At first the linear model was obtained by linear least squares from the raw data. σ was calculated as the root mean square of the residuals. A new linear model was found with weighted regression of least squares using the weights found in equation 5.3. The Huber weights were calculated again using the new linear model and σ. This procedure was repeated until the deviation the new and old model was less than 0.001. A demonstration of the technique is shown in Figure 5.32. We see that the least square regression line is affected by the outliers while the regression line with Huber weights is not.
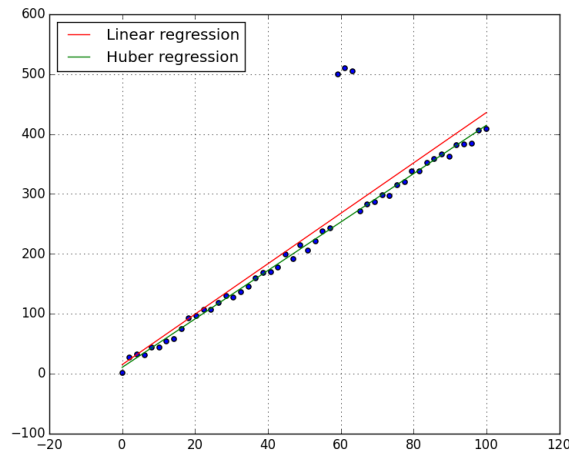
FIGURE 5.32: Simple linear regression (red line) is sensitive to outliers and gives a different regression than expected. Regression using Huber weights (green line) gives model closer to the inliers

If the conjugate point between the hemispheres have identical equivalent currents we expect a slope equal to one in equation (5.2). Furthermore, if the current systems are dependent on B we would also suspect a slope near unity if the conjugate points had

equal magnetic field strengths. We tested this by comparing the ratio of the magnetic perturbations ($\delta B_{SH}/\delta B_{NH}$) to the magnetic field strengths (B_{SH}/B_{NH}). The former ratio can be determined from the slope found in equation (5.2) by rearranging the terms such that $b = \delta B_{SH}/\delta B_{NH}$. The magnetic field strength at the location of the magnetometer stations were calculated using equation (4.6) from the IGRF model. These ratios were calculated for each station pair and the results can be found in Figure 5.33. If a station in NH had more than one conjugate station, an average slope was calculated. Numerical values of the slopes, correlation coefficients and number of data is shown in Table 5.2

Stations	r	r^2	b_{qd}	b_{sm}	N
SCO-B10	0.577	0.332	1.265	0.998	42545
NAQ-B12	0.808	0.653	1.157	0.853	204050
FHB-B14	0.800	0.640	1.181	0.907	67881
GHB-B15	0.767	0.588	1.230	0.969	90568
GHB-B16	0.791	0.626	1.164	0.948	25569
GHB-B17	0.742	0.551	1.167	0.949	75977
GHB-B18	0.772	0.595	1.108	0.909	117175
SKT-B19	0.746	0.557	1.081	0.872	132601
IQA-B19	0.621	0.386	0.812	0.824	97077
STF-B19	0.656	0.431	1.029	0.862	106113
CY0-B20	0.727	0.528	0.786	0.842	4700
UPN-B20	0.659	0.434	0.609	0.641	37187
PGC-B21	0.500	0.250	0.655	0.524	11942
ATU-B21	0.680	0.462	0.965	0.812	73199
GDH-B22	0.671	0.450	0.763	0.659	103022
UMQ-B22	0.546	0.298	0.608	0.569	42304
IQA-B23	0.722	0.522	0.867	0.872	94158
HRN-DVS	0.686	0.470	0.689	0.734	136130
LYR-DVS	0.688	0.473	0.775	0.811	100314
JAN-MAW	0.786	0.618	1.011	0.815	329693
KOT-MCQ	0.846	0.716	0.764	0.745	34798
GDH-PG2	0.671	0.450	0.758	0.641	10183
UMQ-PG2	0.546	0.298	0.710	0.594	8772
PGC-SPA	0.585	0.342	0.738	0.800	52363

TABLE 5.2: Statistical information of each SuperMAG magnetometer pair. r is the correlation coefficient, N is the number of data point in each data set and b_{QD} and b_{SM} are the slopes given in QD and SuperMAG coordinates respectively
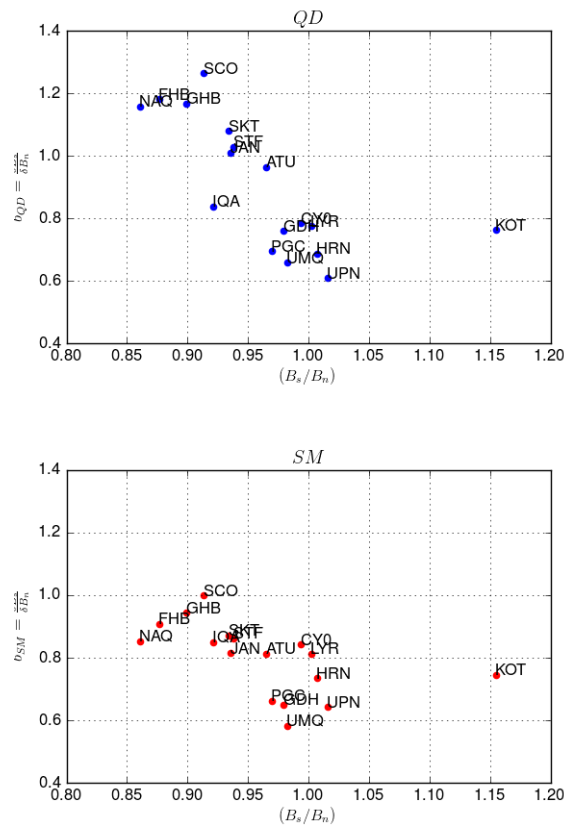
FIGURE 5.33: Ratio of magnetic field strength compared to the strength of magnetic perturbations. The upper figure shows the ratios given in QD-coordinates while the lower figure shows a equivalent plot given in SuperMAG-coordinates
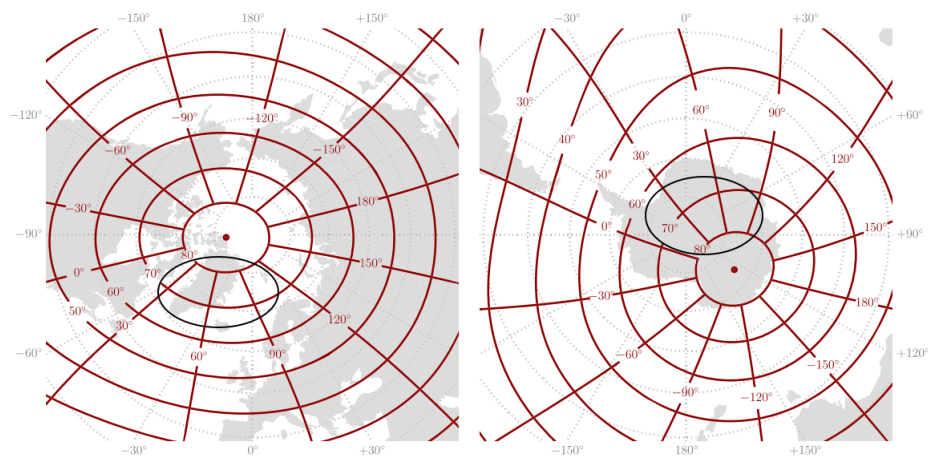
FIGURE 5.34: Contours of QD-coordinates at 0km altitude. The black circles indicate where a majority of the magnetometer stations in our analysis are found.
Figure from Laundal and Richmond [42]

The QD-coordinate system is designed to remove effects from the local magnetic field. In order to demonstrate this, consider an electrojet flowing strictly in QD-coordinates.

Such a current would produce constant N_{qd} perturbations along the same QD longitude. The current may flow over regions with varying local magnetic field and from equation 4.18 we can see that the QD base vectors acts to scale the N_{qd} component to be constant over varying local magnetic fields (Laundal and Gjerloev [41]). Other coordinate systems, such as the NEZ-coordinate system used by SuperMAG, does not compensate for features in the local magnetic field and magnetic perturbations would have a longitudinal dependences even though the current density remains constant. In Figure 5.33 we can see the differences in magnetic perturbations due to magnetic coordinate systems.

A large section of magnetometers in SH was found in a region with weaker magnetic field (black circle in the left map in Figure 5.34) compared to the magnetic field in the region of magnetometer stations found in NH (black circle in the left map in Figure 5.34). Due to the weaker magnetic field the current density measured in SuperMAG components would decrease, but QD-components compensate for this effect. This explains why the $\delta B_{SH}/\delta B_{NH}$ have higher values in QD components than SuperMAG components, which is shown in Figure 5.33.

Even though QD-coordinates removes effects of features in the magnetic field, it does not remove conductivity effects. Ionospheric conductivity depends of the magnetic field strength both directly and by altering the gyration frequency. Conductance is roughly inversely proportional with magnetic field strength and ionospheric currents and also magnetic perturbations would be expected to be stronger at weaker magnetic fields. This is consistent with the result we found in Figure 5.33 and we therefore interpret this as conductivity effects.

We assume that magnetic perturbation measured on the ground is proportional to the strength of the above current systems which is dependent on the ionospheric conductances which is scaled with the magnetic field strength. We therefore tested whether the data in Figure 5.33 can be fitted on the model

$$\frac{\delta B_{SH}}{\delta B_{NH}} = A \left(\frac{B_{SH}}{B_{NH}} \right)^p \tag{5.4}$$

where p is the scaling factor and A is a constant. Regression analysis gives the parameters

$$A = 0.79 \pm 0.04 \tag{5.5}$$

$$p = -3.0 \pm 0.6 \tag{5.6}$$

A plot of this result is shown in Figure 5.35.
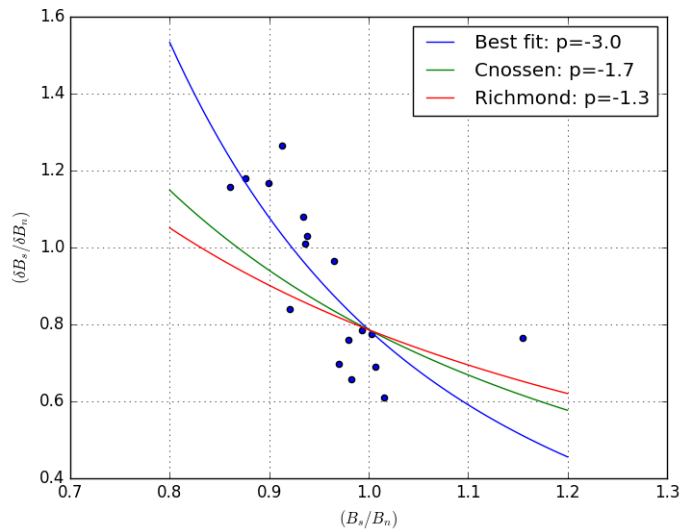
FIGURE 5.35: Scaling factor with all available data

This result is much higher than the scaling factors reported by Richmond [57] and Cnossen et al. [12]. If our result is correct, then it would imply that the ionosphere in darkness has higher dependency of the magnetic field strength than the sunlit ionosphere. However, the precision of the estimated parameters may be questioned. Some of our $b_{qd} = \delta B_{SH}/\delta B_{NH}$ data points were calculated from poorly correlated data sets. The slope is more precisely determined for correlated data.

Low correlations have effects on the slopes and the determination of the scaling factor p. It can be shown that the slope in a linear model is equivalent to $b = r\frac{s_y}{s_x}$ where r is the correlation coefficient and s_x and s_y are the standard deviations of data set $\mathbf{x}$ and $\mathbf{y}$ respectively (Kennedy and Keeping [35]). Low correlation coefficients suppress the value of the slope b_{qd} and a steeper curve must be fitted to the dataset. This give a higher scaling factor than expected. Therefore, we used only high correlated data sets for a more accurate determination of b_{qd} and the scaling factor p. If we required at least half of our data to be explained by linear model, i.e. $r^2 \geq 0.5$, then regression analysis of equation (5.4) gives the parameters

$$A = 0.89 \pm 0.04 \tag{5.7}$$

$$p = -1.9 \pm 0.5 \tag{5.8}$$

Equation (5.4) with parameters A and p given by equations (5.8) and (5.8) is shown in Figure 5.36.
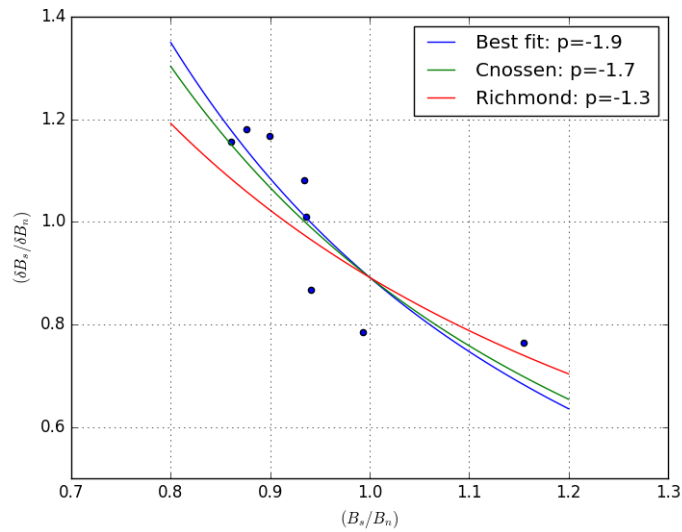
FIGURE 5.36: Plots of equation 5.4 with parameter from our result (blue line) Cnossen et al. [12] (green line) and Richmond [57] (red line). The blue dots are slope from our calculations.

We find that the scaling factor within one standard deviation is equal to $p = [-2.4, -1.4]$. The scaling factor reported by Cnossen et al. [12] is within our results but the scaling factor reported by Richmond [57] is outside. Therefore, we agree with the result reported by Cnossen et al. [12]. However, the model in equation in Figure 5.4 were fitted from only 8 data points. The reliability of this result is therefore questionable. In the calculations of the slope we assumed that the conductances and their corresponding magnetic perturbations were dependent on the strength of the magnetic field, but it depends on other variables as well such as collision frequency. A better method could be using correlation coefficients as weights instead of rejecting data points.

Chapter 6

Summary and Conclusion

We found theoretically that the ionosphere is in darkness for solar zenith angles greater than 100°. However, measurements of magnetic perturbations at magnetic conjugate points suggest that solar zenith angles as low as 80° is low enough to be considered dark. The theoretical value reduced our dataset and we found no advantages in using this value. Therefore, we used solar zenith angles defined by magnetic perturbation measurements.

Many inter-hemispherical asymmetries have been linked to IMF B_y which we have scrutinized using magnetic perturbation data. IMF B_y can cause longitudinal shift of magnetic foot points which optimize magnetic conjugacy. We examined whether this improves correspondence of equivalent currents at conjugate points, but we found the opposite effect. A possible explanation is that other IMF B_y effects such as asymmetric convection and current systems are much more significant.

Theoretical studies suggest that ionospheric conductance is scaled with the strength of the magnetic field, but to our knowledge this has not been tested empirically. Our results were consistent with this and we were able to derive a scaling factor for the night side ionospheric conductance. However, we recommend some caution considering this result.

Chapter 7

Future Work

The statistical significance our analysis can be improved by including more data. This can be done by identify more magnetometer stations at conjugate points or by updating the data in already identified magnetometer stations. Some of our dataset were provided quite recent stations. For example, stations PG1, PG2 and PG3 covered the year 2013 only. For the year to come more data will be provided by SuperMAG and the analysis will be more reliable.

The model fit in section 5.3 should be weighted for a more robust analysis. The determination of the scaling factor were based on regression analysis of data points found by the slope of linear models. The accuracy of calculation of the slopes are dependent on the correlation of the data sets. Therefore, the correlation coefficients could be used as weights in the model fit.

We have treated the magnetic perturbations as a function of the magnetic field strength, because the ionospheric conductances are scaled with the this variable. However, ionospheric conductivity (and conductance) is dependent on both magnetic field and the collision frequency. Therefore, we suggest using multi-variable analysis including both magnetic field strength and collision frequency. By using reasonable assumptions of the altitude of the ionospheric currents, temperature and the ion and electron composition we can estimate the collision frequency by the equation published by Lathuillere and Wickwar [40] or the *International Reference Ionosphere* (Bilitza et al. [5])

In our analysis we assumed that all magnetic perturbation were generated by currents flowing in the ionosphere. However, under certain conditions a significant portion of the magnetic perturbations measured by ground based magnetometers might originate from currents induced from the ground (Tanskanen et al. [64], Viljanen et al. [72]). The ground based magnetometers are placed on different surfaces, such as land, coast and ice, and the surface conductivity might influence the magnetic perturbation measurements. One should therefore separate ionospheric and surface currents, for example by using techniques developed by Pulkkinen et al. [54].

Appendix A

SuperMAG stations

A.1 Location

Pair	Start	End	Hours	Deviation
SCO-B10	2003-02-06	2005-11-22	14020.65	-0.97
NAQ-B12	2001-12-13	2009-01-23	51519.48	-0.92
FHB-B14	2002-01-15	2005-07-25	21299.98	-0.68
GHB-B15	2001-12-17	2005-10-29	26392.62	-0.07
GHB-B16	2005-01-16	2006-08-03	4685.6	-0.49
GHB-B17	2001-12-13	2005-01-16	26477.93	-0.5
GHB-B18	2002-01-16	2006-10-26	32226.33	-0.8
SKT-B19	2002-01-01	2009-01-26	33894.22	-0.48
IQA-B19	2001-12-17	2009-01-26	36042.7	0.99
STF-B19	2001-12-17	2009-01-26	39027.37	-0.72
CY0-B20	2002-01-22	2008-03-08	7640.07	0.76
UPN-B20	2002-01-22	2008-12-18	44644.35	-0.7
PGC-B21	2002-01-19	2002-12-31	8101.2	0.57
ATU-B21	2002-01-19	2007-11-02	31398.92	-0.62
GDH-B22	2002-01-22	2010-01-29	45680.82	-0.59
UMQ-B22	2002-08-15	2010-01-29	35647.33	-0.81
IQA-B23	2002-01-19	2010-01-24	26868.23	0.31
HRN-DVS	1993-01-01	2000-12-30	66740.73	-0.64
LYR-DVS	1996-01-01	2000-12-30	42079.7	-0.78
JAN-MAW	1991-01-01	2005-09-30	115233.93	0.45
KOT-MCQ	1993-11-11	1996-04-20	11417.95	-0.16
UMQ-PG1	2013-01-01	2013-12-30	6273.45	-0.53
GDH-PG2	2013-01-01	2013-12-31	5423.32	0.05
UMQ-PG2	2013-01-01	2013-12-31	4532.3	-0.15
ATU-PG3	2013-01-05	2013-01-08	72.02	0.04
PGC-SPA	1996-08-26	2002-12-31	22614.47	-0.1

TABLE A.1: List of conjugate SuperMAG stations. The columns Start and End tell when the station pairs where operative simultaneously. Date format is given in yyyy-mm-dd. Hours tells when how many hours they were operative simultaneously

IAGA	MLAT	MLON	GLAT	GLON
SCO	71.35	71.95	70.48	338.03
NAQ	65.82	43.16	61.16	314.56
FHB	67.53	38.98	62.0	310.32
GHB	70.12	37.82	64.17	308.27
SKT	71.57	37.22	65.42	307.1
STF	72.73	41.0	67.02	309.28
CY0	78.78	18.51	70.5	291.4
UPN	79.07	40.83	72.78	303.85
PGC	74.36	20.05	66.1	294.2
ATU	74.12	38.31	67.93	306.43
GDH	75.37	39.62	69.25	306.47
UMQ	76.44	42.89	70.68	307.87
IQA	72.52	14.82	63.75	291.48
HRN	73.78	110.45	77.0	15.6
LYR	74.95	112.5	78.2	15.83
JAN	70.17	84.55	70.9	351.3
KOT	64.73	-108.41	66.88	197.4
ATU	73.33	37.31	67.93	306.43

TABLE A.2: Stations in NH. MLAT and MLON are latitude and longitude in magnetic coordinates and GLAT and GLON are latitude and longitude in geographic coordinates. Coordiantes are given in degrees

IAGA	MLAT	MLON	GLAT	GLON
B10	-70.69	57.1	-77.32	39.71
B12	-64.62	29.03	-79.08	335.88
B14	-66.24	28.68	-80.89	337.74
B15	-68.55	36.51	-81.49	2.97
B16	-68.38	30.13	-82.78	347.06
B17	-68.46	30.11	-82.9	347.76
B18	-69.07	25.55	-84.35	336.14
B19	-71.08	29.68	-85.36	2.06
B20	-77.62	29.78	-85.36	95.98
B21	-73.28	28.6	-87.0	28.41
B22	-75.43	30.34	-86.51	68.17
B23	-72.03	19.51	-88.03	316.13
DVS	-74.37	100.2	-68.58	77.97
MAW	-70.01	90.16	-67.61	62.88
MCQ	-64.15	-111.89	-54.5	158.95
PG1	-76.63	33.5	-85.5	77.2
PG2	-75.31	39.11	-84.42	57.96
PG3	-73.47	37.96	-84.42	37.62
SPA	-73.87	18.58	-90.0	0.0

TABLE A.3: Stations in SH. MLAT and MLON are latitude and longitude in magnetic coordinates and GLAT and GLON are latitude and longitude in geographic coordinates. Coordiantes are given in degrees

A.2 Magnetic field strength

IAGA	B
SCO	53004.27
NAQ	54144.0
FHB	54871.3
GHB	55329.79
SKT	55533.75
STF	55304.3
CY0	56946.74
UPN	55707.78
PGC	57101.54
ATU	55634.75
GDH	55610.72
UMQ	55443.41
IQA	57555.11
HRN	53828.83
LYR	54058.14
JAN	52526.43
KOT	55851.77
ATU	55634.75

TABLE A.4: Magnetic field strength at each magnetometer stations according to the IGRF-12 model in NH. Units are given in nT

IAGA	B
B10	48403.87
B12	46606.53
B14	48096.02
B15	48660.94
B16	49592.67
B17	49693.59
B18	51021.84
B19	51876.22
B20	56580.0
B21	53689.81
B22	55018.92
B23	54150.75
DVS	54193.14
MAW	49151.52
MCQ	64500.93
PG1	55415.64
PG2	53892.15
PG3	52518.62
SPA	57075.83

TABLE A.5: Magnetic field strength at each magnetometer stations according to the IGRF-12 model in SH. Units are given in nT

Appendix B

Supplementary Theory

B.1 Maxwell's Equations

Electrodynamics can be summarised by Maxwell's equation:

$$\nabla \cdot \mathbf{E} = \frac{\rho_c}{\epsilon_o} \tag{B.1}$$

$$\nabla \cdot \mathbf{B} = 0 \tag{B.2}$$

$$\nabla \times \mathbf{E} = -\frac{\partial \mathbf{B}}{\partial t} \tag{B.3}$$

$$\nabla \times \mathbf{B} = \mu_0 \mathbf{j} + \mu_0 \epsilon_0 \frac{\partial \mathbf{E}}{\partial t} \tag{B.4}$$

here is $\mathbf{E}$ the electric field, $\mathbf{B}$ is the magnetic field, $\mathbf{j}$ is the current density, ρ_c is the charge density, ϵ_0 is the vacuum permittivity and μ_0 is the permeability of free space.

B.2 Magnetohydrodynamics

Magnetohydrodynamics (MHD) is a field is physics where the interactions between plasma and magnetic fields are studied. MHD describes plasma as a fluid subjected to magnetic forces. In ideal MHD we consider the plasma as having infinite electric conductivity. Using these assumptions one can derive the *Hydrodynamic theorem* which states that

$$\frac{\partial \mathbf{B}}{\partial t} = \nabla \times (\mathbf{v} \times \mathbf{B}) \tag{B.5}$$

where $\mathbf{v}$ is the plasma velocity. An implication of this theorem is that plasma is frozen-in to the magnetic field. It can also be showed that equation (B.5) is equivalent to

$$\mathbf{E} + \mathbf{v} \times \mathbf{B} = 0 \tag{B.6}$$

Equation B.6 can tell us that the electric field in the reference of the moving plasma is equal to zero. Other important equations in MHD are the continuity equation (eq. B.7) and the momentum equation (eq. B.8) which describes the behaviour of a plasma. T

$$\frac{\partial \rho \mathbf{v}}{\partial t} + \nabla \cdot (\rho \mathbf{v}) = 0 \tag{B.7}$$

$$\rho \left(\frac{\partial}{\partial t} + \mathbf{v} \cdot \nabla \right) \mathbf{v} = -\nabla \cdot \mathbf{P} + \mathbf{j} \times \mathbf{B} \tag{B.8}$$

where $\mathbf{P}$ is the pressure tensor and ρ is mass density. The continuity equation tells us that mass is conserved. The first term in the momentum equation is pressure force and the second term is the magnetic force. MHD is used extensively in space physics and can be used to describe plasma behaviour in the solar wind and in the ionosphere.

Bibliography

[1] S.-I. Akasofu. The development of the auroral substorm. *Planetary and Space Science*, 12(4):273–282, 1964. ISSN 00320633. doi: 10.1016/0032-0633(64)90151-5. URL `http://www.sciencedirect.com/science/article/pii/0032063364901515{%}5Cnhttp://linkinghub.elsevier.com/retrieve/pii/0032063364901515`.

[2] Hannes Alfvén. Existence of electromagnetic-hydrodynamic waves. *Nature*, 150 (3805):405–406, 1942.

[3] J. H. Allen and H. W. Kroehl. Spatial and temporal distributions of magnetic effects of auroral electrojets as derived from AE indices. *Journal of Geophysical Research*, 80(3667):55–62, 1975.

[4] Wolfgang Baumjohann and Rudolf A Treumann. *Basic Space Plasma Physics*. Imperial College Press, 1996. ISBN 1-86094-017-X.

[5] Dieter Bilitza, David Altadill, Yongliang Zhang, Chris Mertens, Vladimir Truhlik, Phil Richards, Lee-Anne McKinnell, and Bodo Reinisch. The International Reference Ionosphere 2012 a model of international collaboration. *Journal of Space Weather and Space Climate*, 4:A07, 2014. ISSN 2115-7251. doi: 10.1051/swsc/2014004. URL `http://www.swsc-journal.org/10.1051/swsc/2014004`.

[6] Kristian Birkeland. *Exp{é}dition norv{é}gienne de 1899-1900 pour l'{é}tude des aurores bor{é}ales: R{é}sultats des recherches magn{é}tiques*. En commission chez J. Dybwad, 1901.

[7] Kristian Birkeland. *The Norwegian aurora polaris expedition 1902-1903*, volume 1. H. Aschelhoug & Company, 1908.

[8] Kristian Birkeland. The Norwegian Aurora Polaris Expedition 1902–1903, vol. 1, On the Cause of Magnetic Storms and the Origin of Terrestrial Magnetism, second section. *H. Aschehoug and Co, Christiania*, 1, 1913.

[9] M. Blanc, R. Kallenbach, and N. V. Erkaev. Solar system magnetospheres. *Space Science Reviews*, 116(1-2):227–298, 2005. ISSN 00386308. doi: 10.1007/s11214-005-1958-y.

[10] S Chapman. The absorption and dissociative or ionizing effect of monochromatic radiation in an atmosphere on a rotating earth part II. Grazing incidence. *Proceedings of the Physical Society*, 43(5):483–501, 1931. ISSN 0959-5309. doi: 10.1088/0959-5309/43/5/302. URL `http://stacks.iop.org/0959-5309/43/i=5/a=302?key=crossref.382ab6545d3e0beb489e562d020ea94f`.

[11] Sydney Chapman and Majid Mian. The rate of ion-production at any height in the Earth's atmosphere: IThe spherical harmonic representation of its worldwide distribution. *Proceedings of the Physical Society*, 47(1):31–38, 1942. doi: 10.1029/TE047i001p00031.

[12] Ingrid Cnossen, Arthur D. Richmond, Michael Wiltberger, Wenbin Wang, and Peter Schmitt. The response of the coupled magnetosphere-ionosphere-thermosphere system to a 25% reduction in the dipole moment of the Earth's magnetic field. *Journal of Geophysical Research: Space Physics*, 116(12):1–13, 2011. ISSN 21699402. doi: 10.1029/2011JA017063.

[13] S. W H Cowley. Magnetospheric asymmetries associated with the y-component of the IMF. *Planetary and Space Science*, 29(1):79–96, jan 1981. ISSN 00320633. doi: 10.1016/0032-0633(81)90141-0. URL `http://linkinghub.elsevier.com/retrieve/pii/0032063381901410`.

[14] S. W. H. Cowley and M. Lockwood. Excitation and decay of solar wind-driven flows in the magnetosphere-ionosphere system. *Annales geophysicae*, 10 (1-2):103–115, 1992. ISSN 0992-7689. URL `https://www.mendeley.com/research/excitation-decay-solar-winddriven-flows-magnetosphereionophere-system/?utm{_}source=desktop{&}utm{_}medium=1.15.2{&}utm{_}campaign=open{_}catalog{&}userDocumentId={%}7B33adb3bf-7283-4275-b9ad-f6d5f56b7b65{%}7D`.

[15] S W H Cowley, J P Morelii, and M Lockwood1. Dependence of Convective Flows and Particle Precipitation in the High-Latitude Dayside Ionosphere on the X and Y Components of the Interplanetary Magnetic Field. *JOURNAL OF GEOPHYSICAL RESEARCH*, 96(A4):5557–5564, 1991.

[16] T. Neil Davis and Masahisa Sugiura. Auroral electrojet activity index AE and its universal time variations. *Journal of Geophysical Research*, 71(3): 785–801, 1966. ISSN 01480227. doi: 10.1029/JZ071i003p00785. URL `http://onlinelibrary.wiley.com/doi/10.1029/JZ071i003p00785/full{%}5Cnhttp://doi.wiley.com/10.1029/JZ071i003p00785`.

[17] J. W. Dungey. Interplanetary magnetic field and the auroral zones. *Physical Review Letters*, 1961. ISSN 00319007. doi: 10.1103/PhysRevLett.6.47.

[18] J T Emmert, A D Richmond, and D P Drob. A computationally compact representation of magnetic-apex and Quasi-Dipole coordinates with smooth base vectors. *Journal of Geophysical Research: Space Physics*, 115(8):1–13, 2010. ISSN 21699402. doi: 10.1029/2010JA015326.

[19] M. H. MH Farris and C. T. Russell. Determining the standoff distance of the bow shock: Mach number dependence and use of models. *Journal of Geophysical Research: ...*, 99(A9):17681–17689, 1994. ISSN 0148-0227. doi: 10.1029/94JA01020. URL http://onlinelibrary.wiley.com/doi/10.1029/94JA01020/full.

[20] Y. I. Feldstein. Auroral morphology, I. The location of the auaroral zone. *Tellus*, 16 (2):252–257, 1964. ISSN 00402826. doi: 10.1111/j.2153-3490.1964.tb00163.x. URL http://doi.wiley.com/10.1111/j.2153-3490.1964.tb00163.x.

[21] E Friis-Christensen, Y Kamide, A D Richmond, and S Matsushita. Interplanetary magnetic field control of high-latitude electric fields and currents determined from Greenland Magnetometer Data. *Journal of Geophysical Research*, 90(A2):1325–1338, 1985. ISSN 0148-0227. doi: 10.1029/JA090iA02p01325.

[22] E. Friis-Christensen, C. C. Finlay, M. Hesse, and K. M. Laundal. Magnetic Field Perturbations from Currents in the Dark Polar Regions During Quiet Geomagnetic Conditions. *Space Science Reviews*, pages 281–297, 2017. ISSN 0038-6308. doi: 10.1007/s11214-017-0332-1. URL http://link.springer.com/10.1007/s11214-017-0332-1.

[23] N Fukushima. Some topics and historical episodes in geomagnetism and aeronomy. *Journal of Geophysical Research*, 99(A10):19113–19142, 1994. ISSN 0148-0227. doi: 10.1029/94JA00102.

[24] Naoshi Fukushima. EQUIVALENCE IN GROUND GEOMAGNETIC EFFECT OF CHAPMAN–VESTINE'S AND BIRKELAND–ALFVEN'S ELECTRIC CURRENT-SYSTEMS FOR POLAR MAGNETIC STORMS. *Rep. Ionosphere Space Res. Jap.*, 23:219–227, 1969.

[25] Naoshi Fukushima. Generalized theorem for no ground magnetic effect of vertical currents connected with Pedersen currents in the uniform-conductivity ionospherele. *Report of Ionosphere and Space Research in Japan*, 30:35–40, 1976.

[26] S Gasda and A D Richmond. Longitudinal and interhemispheric variations of auroral ionospheric electrodynamics in a realistic geomagnetic field. *J. Geophys.*

Res., 103(A3):4011–4021, 1998. ISSN 0148-0227. doi: 10.1029/97ja03243. URL `http://dx.doi.org/10.1029/97JA03243`.

[27] J W Gjerloev. The SuperMAG data processing technique. *Journal of Geophysical Research: Space Physics*, 117(9):1–19, 2012. ISSN 21699402. doi: 10.1029/2012JA017683.

[28] J W Gjerloev and R A Hoffman. Currents in auroral substorms. *Journal of Geophysical Research: Space Physics*, 107(A8), 2002. ISSN 21699402. doi: 10.1029/2001JA000194.

[29] L. Harang. The mean field of disturvance of polar geomagnetic storms. *Journal of Geophysical Research*, 51(3):353–380, 1946.

[30] J P Heppner. Polar-cap electric field distributions related to the interplanetary magnetic field direction. *J. Geophys. Res.*, 77(25):4877–4887, 1972. ISSN 01480227. doi: 10.1029/JA077i025p04877. URL `http://doi.wiley.com/10.1029/JA077i025p04877`.

[31] Peter J. Huber. Robust Estimation of a Location Parameter. *The Annals of Mathematical Statistics*, 35(1):73–101, 1964. ISSN 0003-4851. doi: 10.1214/aoms/1177703732.

[32] T. Iijima and T. A. Potemra. Large-scale characteristics of field-aligned currents associated with substorms. *Journal of Geophysical Research*, 83(A2):599, 1978. ISSN 0148-0227. doi: 10.1029/JA083iA02p00599. URL `http://doi.wiley.com/10.1029/JA083iA02p00599`.

[33] Y. Kamide and S. I Akasofu. Notes on the auroral electrojet indices. *Reviews of Geophysics*, 21(7):1647–1656, 1983. ISSN 19449208. doi: 10.1029/RG021i007p01647.

[34] Michael C Kelly. *The Earth's Ionosphere*. Academic Press, 2 edition, 2009. ISBN 9780120884254.

[35] J. F. Kennedy and E. S. Keeping. Mathematics of Statistics. In *Linear Regression and Correlation*, chapter 15, pages 252–285. 3 edition, 1962.

[36] Jerry L. Kisabeth and Gordon Rostoker. Development of the polar electrojet during polar magnetic substorms. *Journal of Geophysical Research*, 76(28):6815, 1971. ISSN 0148-0227. doi: 10.1029/JA076i028p06815.

[37] Margaret Galland Kivelson. Planetary magnetospheres. *Handbook of Solar-Terrestrial Environment*, pages 469–492, 2007. ISSN 01679295. doi: 10.1007/978-3-540-46315-3_19.

[38] Hannu E J Koskinen and Tuija I Pulkldnen. Midnight velocity shear zone and the concept of Harang discontinuity. *Journal of Geophysical Research*, 100(A6): 9539–9547, 1995.

[39] T Kunkel, J Untiedt, W Baumjohann, and R A Greenwald. Electric fields and currents at the Harang discontinuity-A case study. *Journal of Geophysics Zeitschrift Geophysik*, 59:73–86, 1986.

[40] Chantal Lathuillere and Vincent B Wickwar. Incoherent Scatter Measurements of Ion-Neutral Collision Frequencies and Temperatures in the Lower Thermosphere of the Auroral Region. *JOURNAL OF GEOPHYSICAL RESEARCH*, 88144(1): 137–10, 1983. doi: 10.1029/JA088iA12p10137.

[41] K M Laundal and J W Gjerloev. What is the appropriate coordinate system for magnetometer data when analyzing ionospheric currents? *Journal of Geophysical Research A: Space Physics*, 2014. ISSN 21699402. doi: 10.1002/2014JA020484.

[42] K M Laundal and A D Richmond. Magnetic Coordinate Systems, 2016. ISSN 15729672.

[43] K. M. Laundal, S. E. Haaland, N. Lehtinen, J. W. Gjerloev, N. Østgaard, P. Tenfjord, J. P. Reistad, K. Snekvik, S. E. Milan, S. Ohtani, and B. J. Anderson. Birkeland current effects on high-latitude ground magnetic field perturbations. *Geophysical Research Letters*, 2015. ISSN 19448007. doi: 10.1002/2015GL065776.

[44] K. M. Laundal, J. W. Gjerloev, N. Østgaard, J. P. Reistad, S. Haaland, K. Snekvik, P. Tenfjord, S. Ohtani, and S. E. Milan. The impact of sunlight on high-latitude equivalent currents. *Journal of Geophysical Research A: Space Physics*, 121(3): 2715–2726, 2016. ISSN 21699402. doi: 10.1002/2015JA022236.

[45] G Le, J a. Slavin, and R J Strangeway. Space Technology 5 observations of the imbalance of regions 1 and 2 field-aligned currents and its implication to the cross-polar cap Pedersen currents. *Journal of Geophysical Research*, 115(A7):A07202, 2010. ISSN 0148-0227. doi: 10.1029/2009JA014979. URL `http://doi.wiley.com/10.1029/2009JA014979`.

[46] K. Liou and P. T. Newell. On the azimuthal location of auroral breakup: Hemispheric asymmetry. *Geophysical Research Letters*, 37(23):1–5, 2010. ISSN 00948276. doi: 10.1029/2010GL045537.

[47] Johann Lutjeharms, Isabelle Ansorge, Marten Gründlingh, Roy van Ballegooyen, Scarla Weeks, Eric Machu, and Olaf Boebel. Comment on New Global Drifter Data Set Available. *Eos, Transactions American Geophysical Union*, 85(19):2004, 2004.

ISSN 0096-3941. doi: 10.1029/2004EO190008. URL `http://www.agu.org/pubs/crossref/2004/2004EO190008.shtml`.

[48] S E Milan, M Lester, S W H Cowley, K Oksavik, M Brittnacher, G Sofko, J Villain, S E Milan, M Lester, S W H Cowley, K Oksavik, and M Brittnacher. Variations in the polar cap area during two substorm cycles To cite this version : Annales Geophysicae Variations in the polar cap area during two substorm cycles. *Ann. Geophys*, 21(5):1121–1140, 2003.

[49] Jøran Moen and Asgeir Brekke. The solar flux influence on quiet time conductances in the auroral ionosphere. *Geophysical Research Letters*, 20(10):971, 1993. ISSN 0094-8276. doi: 10.1029/92GL02109.

[50] N. Østgaard, S. B. Mende, H. U. Frey, T. J. Immel, L. A. Frank, J. B. Sigwarth, and T. J. Stubbs. Interplanetary magnetic field control of the location of substorm onset and auroral features in the conjugate hemispheres. *Journal of Geophysical Research: Space Physics*, 109(A7), 2004. ISSN 21699402. doi: 10.1029/2003JA010370.

[51] N Østgaard, K M Laundal, L Juusola, A Åsnes, S E Håland, and J M Weygand. Interhemispherical asymmetry of substorm onset locations and the interplanetary magnetic field. *Geophysical Research Letters*, 38(8):1–5, 2011. ISSN 00948276. doi: 10.1029/2011GL046767.

[52] E. N. Parker. Dynamics of the Interplanetary Gas and Magnetic Fields. *The Astrophysical Journal*, 128:664, 1958. ISSN 0004-637X. doi: 10.1086/146579.

[53] E N Parker. The alternative paradigm for magnetospheric physics. *Journal of Geophysical Research*, 101(A5):10587–10625, 1996.

[54] Antti Pulkkinen, Olaf Amm, and Ari Viljanen. Separation of the geomagnetic variation field on the ground into external and internal parts using the spherical elementary current system method. *Earth, Planets and Space*, 2003. ISSN 13438832.

[55] M. H. Rees. Physics and chemistry of the upper atmosphere. 1989.

[56] A D Richmond. Ionospheric Electrodynamics Using Magnetic Apex Coordinates. *Journal of geomagnetism and geoelectricity*, 47(2):191–212, 1995. ISSN 0022-1392. doi: 10.5636/jgg.47.191.

[57] Arthur D Richmond. Handbook of Atmospheric Electrodynamics. In *CRC Press*, volume 2, page 260. 1995.

[58] R M Robinson and R R Vondrak. Region Ionization and Conductivity Produced By Solar Illumination At High Latitudes. *Journal of Geophysical Research*, 89(4):3951, 1984. ISSN 0148-0227. doi: 10.1029/JA089iA06p03951.

[59] G Rostoker, S I Akasofu, J Foster, R A Greenwald, Y Kamide, K Kawasaki, A T Y Lui, R L McPherron, and C T Russell. Magnetospheric Substorms - Definition and Signatures. *J. Geophys. Res.*, 85(A4):1663–1668, 1980. ISSN 0148-0227. doi: 10.1029/JA085iA04p01663. URL http://dx.doi.org/10.1029/JA085iA04p01663.

[60] Gordon Rostoker. Polar Magnetic Substorms. *Reviews of Geophysics*, 10(1):157–211, 1972. ISSN 19449208. doi: 10.1029/RG010i001p00157.

[61] C T Russell. Geophysical coordinate transformations. *Cosmic electrodynamics*, 2: 184–196, 1971. ISSN 0010-9509.

[62] J.-H. Shue, J. K. Chao, H. C. Fu, C. T. Russell, P. Song, K. K. Khurana, and H. J. Singer. A new functional form to study the solar wind control of the magnetopause size and shape. *Journal of Geophysical Research: Space Physics*, 102(A5):9497–9511, 1997. ISSN 01480227. doi: 10.1029/97JA00196. URL http://doi.wiley.com/10.1029/97JA00196.

[63] Edward J. Smith. The heliospheric current sheet. *Journal of Geophysical Research: Space Physics*, 106(A8):15819–15831, aug 2001. ISSN 01480227. doi: 10.1029/2000JA000120. URL http://doi.wiley.com/10.1029/2000JA000120.

[64] E I Tanskanen, A Viljanen, T I Pulkkinen, R Pirjola, L Häkkinen, A Pulkkinen, and O Amm. At substorm onset, 40% of AL comes from underground. *Journal of Geophysical Research: Space Physics*, 106(A7):13119–13134, 2001. ISSN 0148-0227. doi: 10.1029/2000ja900135. URL http://dx.doi.org/10.1029/2000JA900135.

[65] P. Tenfjord, N. Østgaard, K. Snekvik, K. M. Laundal, J. P. Reistad, S. Haaland, and S. E. Milan. How the IMF By induces a By component in the closed magneto-sphere and how it leads to asymmetric currents and convection patterns in the two hemispheres. *Journal of Geophysical Research A: Space Physics*, 120(11):9368–9384, 2015. ISSN 21699402. doi: 10.1002/2015JA021579.

[66] Erwan Thébault, C.D. Beggan, C.C. Finlay, and ... International Geomagnetic Reference Field: the 12th generation. *Earth, Planets and Space*, 67(1):67–79, 2015. doi: 10.1186/s40623-015-0228-9.

[67] J Untiedt and W Baumjohann. Studies of polar current systems using the IMS Scandinavian magnetometer array. *Space Science Reviews*, 63(3):245–390, 1993. ISSN 1572-9672. doi: 10.1007/BF00750770. URL http://dx.doi.org/10.1007/BF00750770.

[68] T. E. Vanzandt, W L Clark, and J. M. Warnock. Magnetic apex coordinates: A magnetic coordinate system for the ionospheric F2 layer. *Journal of Geophysical*

Research, 77(13):2406–2411, 1972. doi: 10.1029/JA077i013p02406. URL `http://adsabs.harvard.edu/abs/1972JGR....77.2406V`.

[69] V. M. Vasyliunas. The mechanical advantage of the magnetosphere: solar-wind-related forces in the magnetosphere-ionosphere-Earth system. *Ann. Geophys*, 25: 255–269, 2007. ISSN 1432-0576. doi: 10.5194/angeo-25-255-2007. URL `www.ann-geophys.net/25/255/2007/`.

[70] Vytenis M. Vasyliunas. Physics of magnetospheric variability. *Space Science Reviews*, 158(1):91–118, 2011. ISSN 00386308. doi: 10.1007/s11214-010-9696-1.

[71] James F. Vickrey, Richard R. Vondrak, and Stephen J. Matthews. The diurnal and latitudinal variation of auroral zone ionospheric conductivity. *Journal of Geophysical Research*, 86(80):65, 1981. ISSN 0148-0227. doi: 10.1029/JA086iA01p00065.

[72] Ari Viljanen, Kirsti Kauristie, and Kari Pajunp???? On induction effects at EISCAT and IMAGE magnetometer stations. *Geophysical Journal International*, 1995. ISSN 1365246X. doi: 10.1111/j.1365-246X.1995.tb06446.x.

[73] D R Weimer, D M Ober, N C Maynard, W J Burke, M R Collier, D J McComas, N F Ness, and C W Smith. Variable time delays in the propagation of the interplanetary magnetic field. *Journal of Geophysical Research: Space Physics*, 107(A8), 2002. ISSN 21699402. doi: 10.1029/2001JA009102.

[74] D. R. Weimer, D. M. Ober, N. C. Maynard, M. R. Collier, D. J. McComas, N. F. Ness, C. W. Smith, and J. Watermann. Predicting interplanetary magnetic field (IMF) propagation delay times using the minimum variance technique. *Journal of Geophysical Research: Space Physics*, 108(A1):1–12, 2003. ISSN 21699402. doi: 10.1029/2002JA009405.

[75] J. M. Weygand, E. Zesta, and O. Troshichev. Auroral electrojet indices in the Northern and Southern Hemispheres: A statistical comparison. *Journal of Geophysical Research: Space Physics*, 119(6):4819–4840, 2014. ISSN 21699402. doi: 10.1002/2013JA019377.